HAL
open science

TOI-2196 b: Rare planet in the hot Neptune desert transiting a G-type star

Carina M. Persson, Iskra Y. Georgieva, Davide Gandolfi, Lorena Acuna, Artem Aguichine, Alexandra Muresan, Eike Guenther, John Livingston, Karen A. Collins, Fei Dai, et al.

To cite this version:

Carina M. Persson, Iskra Y. Georgieva, Davide Gandolfi, Lorena Acuna, Artem Aguichine, et al.. TOI-2196 b: Rare planet in the hot Neptune desert transiting a G-type star. Astronomy and Astrophysics - A&A, 2022, 666, 10.1051/0004-6361/202244118 . insu-03863236

HAL Id: insu-03863236

https://insu.hal.science/insu-03863236v1

Submitted on 21 Nov 2022

HAL is a multi-disciplinary open access archive for the deposit and dissemination of scientific research documents, whether they are published or not. The documents may come from teaching and research institutions in France or abroad, or from public or private research centers.

L'archive ouverte pluridisciplinaire **HAL**, est destinée au dépôt et à la diffusion de documents scientifiques de niveau recherche, publiés ou non, émanant des établissements d'enseignement et de recherche français ou étrangers, des laboratoires publics ou privés.

Distributed under a Creative Commons Attribution 4.0 International License

A&A 666, A184 (2022)
https://doi.org/10.1051/0004-6361/202244118
© C. M. Persson et al. 2022

Astronomy & Astrophysics

TOI-2196 b: Rare planet in the hot Neptune desert transiting a G-type star

Carina M. Persson[1], Iskra Y. Georgieva[1], Davide Gandolfi[2], Lorena Acuña[3], Artem Aguichine[3], Alexandra Muresan[4], Eike Guenther[5], John Livingston[6,7,8], Karen A. Collins[9], Fei Dai[10], Malcolm Fridlund[1,11], Elisa Goffo[2,5], James S. Jenkins[12,13], Petr Kabáth[14], Judith Korth[4], Alan M. Levine[15], Luisa M. Serrano[2], José Vines[13], Oscar Barragán[16], Ilaria Carleo[17], Knicole D. Colon[18], William D. Cochran[19], Jessie L. Christiansen[20], Hans J. Deeg[17,21], Magali Deleuil[3], Diana Dragomir[22], Massimiliamo Esposito[5], Tianjun Gan[23], Sascha Grziwa[24], Artie P. Hatzes[5], Katharine Hesse[15], Keith Horne[25], Jon M. Jenkins[26], John F. Kielkopf[27], P. Klagyivik[28], Kristine W. F. Lam[29], David W. Latham[9], Rafa Luque[30], Jaume Orell-Miquel[17,21], Annelies Mortier[31,32], Olivier Mousis[3], Noria Narita[6,17,33], Hannah L. M. Osborne[34], Enric Palle[17], Riccardo Papini[35], George R. Ricker[15], Hendrik Schmerling[24], Sara Seager[15,36,37], Keivan G. Stassun[38], Vincent Van Eylen[34], Roland Vanderspek[15], Gavin Wang[39], Joshua N. Winn[40], Bill Wohler[26,41], Roberto Zambelli[42], and Carl Ziegler[43]

(Affiliations can be found after the references)

Received 25 May 2022 / Accepted 11 July 2022

ABSTRACT

The hot Neptune desert is a region hosting a small number of short-period Neptunes in the radius–instellation diagram. Highly irradiated planets are usually either small ($R \lesssim 2\ R_\oplus$) and rocky or they are gas giants with radii of $\gtrsim 1\ R_J$. Here, we report on the intermediate-sized planet TOI-2196 b (TIC 372172128.01) on a 1.2 day orbit around a G-type star ($V = 12.0$, [Fe/H] = 0.14 dex) discovered by the Transiting Exoplanet Survey Satellite in sector 27. We collected 41 radial velocity measurements with the HARPS spectrograph to confirm the planetary nature of the transit signal and to determine the mass. The radius of TOI-2196 b is $3.51 \pm 0.15\ R_\oplus$, which, combined with the mass of $26.0 \pm 1.3\ M_\oplus$, results in a bulk density of $3.31^{+0.51}_{-0.43}$ g cm^{-3}. Hence, the radius implies that this planet is a sub-Neptune, although the density is twice than that of Neptune. A significant trend in the HARPS radial velocity measurements points to the presence of a distant companion with a lower limit on the period and mass of 220 days and 0.65 M_J, respectively, assuming zero eccentricity. The short period of planet b implies a high equilibrium temperature of 1860 ± 20 K, for zero albedo and isotropic emission. This places the planet in the hot Neptune desert, joining a group of very few planets in this parameter space discovered in recent years. These planets suggest that the hot Neptune desert may be divided in two parts for planets with equilibrium temperatures of $\gtrsim$1800 K: a hot sub-Neptune desert devoid of planets with radii of $\approx$1.8–3 $R_\oplus$ and a sub-Jovian desert for radii of $\approx$5–12 $R_\oplus$. More planets in this parameter space are needed to further investigate this finding. Planetary interior structure models of TOI-2196 b are consistent with a H/He atmosphere mass fraction between 0.4% and 3%, with a mean value of 0.7% on top of a rocky interior. We estimated the amount of mass this planet might have lost at a young age and we find that while the mass loss could have been significant, the planet had not changed in terms of character: it was born as a small volatile-rich planet and it remains one at present.

Key words. planets and satellites: composition – planetary systems – planets and satellites: detection – planets and satellites: individual: TOI-2196 – techniques: photometric – techniques: radial velocities

1. Introduction

With the large number of *Kepler* (Borucki et al. 2010) planets, evidence of a bimodal population has emerged, made up of small planets with a gap in the size distribution between ~1.5 and 2 $R_\oplus$, often referred to as the radius gap (Fulton et al. 2017; Van Eylen et al. 2018, 2021; Petigura et al. 2022). This feature was predicted before the observational discovery by several groups as a result of envelope mass loss due to photoevaporation (Lopez & Fortney 2013; Owen & Wu 2013; Jin et al. 2014; Chen & Rogers 2016). Other studies have shown that core-powered envelope mass loss could also carve out a gap in the radius distribution of small planets (Ginzburg et al. 2018; Gupta & Schlichting 2019).

The two populations on either side of the radius gap are: super-Earths, commonly defined as having radii of $1.2 \lesssim R/R_\oplus \lesssim 1.7$ and believed to be mainly rocky, and volatile-rich sub-Neptunes with radii of $1.7 \lesssim R/R_\oplus \lesssim 4$. According to available models, a part of the super-Earth population could, in fact, be remnant cores of sub-Neptunes stripped of their atmospheres. Consequently, mass loss plays an important role in the first few hundred million years of exoplanet evolution (Adams & Laughlin 2006; Kubyshkina et al. 2018).

Despite the abundance of small planets, there is a dearth of hot sub-Neptunes and Neptunes in the radius–instellation (or equilibrium temperature) diagram, namely, the so-called hot Neptune desert or sub-Jovian desert (Szabó & Kiss 2011; Benítez-Llambay et al. 2011; Sanchis-Ojeda et al. 2014; Mazeh et al. 2016), or (otherwise) the hot super-Earth desert as referred to by Lundkvist et al. (2016) for smaller planets with radii between 2.2 and 3.8 $R_\oplus$. The observed period distribution already drops for $P_{\rm orb} < 3$ days despite a strong selection bias due to easy detection which indicates that short period planets are rare. Most planets facing high instellation are either small and rocky with

Open Access article, published by EDP Sciences, under the terms of the Creative Commons Attribution License (https://creativecommons.org/licenses/by/4.0), which permits unrestricted use, distribution, and reproduction in any medium, provided the original work is properly cited.
This article is published in open access under the Subscribe-to-Open model. Subscribe to A&A to support open access publication.

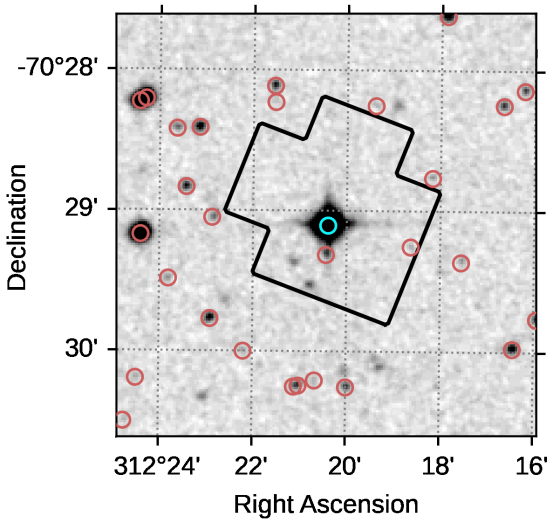

Fig. 1. $3' \times 3'$ DSS2 image (red filter) centered on TOI-2196 (cyan circle). The SPOC photometric aperture of sector 27 is outlined in black while *Gaia* DR2 sources within $2'$ from the target are marked by the red circles.

masses below 10 $M_\oplus$ and radii $\lesssim 2\ R_\oplus$, or massive gas giants with radii $\gtrsim 1\ R_J$.

Up until a few years ago, the hot Neptune desert was almost completely empty in terms of observed planets. New discoveries have begun to uncover a population of planets in the desert, although their small number does not allow for the exact circumstances of their existence to be defined. High precision radius and mass measurements of these planets are crucial to constrain theoretical models of their formation and evolution. The lack of planets in this parameter space suggests difficulties of retaining an extended atmosphere in strong irradiation environments (Lopez & Fortney 2014), possibly indicating different formation and evolution mechanisms, or high-eccentricity migration (Mazeh et al. 2013; Owen & Lai 2018).

Within the hot Neptune desert, there are currently only three known planets with equilibrium temperatures above 1800 K[1], corresponding to a 1.3 day orbit for sun-like stars, with a precision of 10% and 30% or better in measured radii and masses: K2-100 b (Barragán et al. 2019a), TOI-849 b (Armstrong et al. 2020), and LTT 9779 b (Jenkins et al. 2020b). Two additional planets with radii measured to a precision of 10% or better but without measured masses are also known: K2-278 b (Livingston et al. 2018) and Kepler-644 b (Berger et al. 2018).

This paper presents the discovery and characterisation of the intermediate-sized planet TOI-2196 b (TIC 372172128.01) in the hot Neptune desert discovered by The Transiting Exoplanet Survey Satellite (TESS; Ricker et al. 2015) in 2020. Following the discovery, our international KESPRINT[2] collaboration performed follow-up radial velocity observations of this planet candidate to confirm the planetary nature and determine its mass. The star's equatorial coordinates together with other basic parameters are listed in Table 1.

We present the observations in Sect. 2 and the data analysis in Sect. 3. In Sect. 4, we discuss the hot Neptune desert, the planet interior, and atmospheric mass loss. We end the paper with our conclusions in Sect. 5.

[1] Assuming a Bond albedo of zero and a heat redistribution factor of unity (isotropic emission).

[2] KESPRINT is an international consortium devoted to the characterisation and research of exoplanets discovered with space-based missions, http://kesprint.science

Table 1. Basic parameters for TOI-2196.

Parameter	Value
Main identifiers	
TIC	372172128
2MASS	J20492158-7029058
WISE	J204921.59-702906.1
TYC	9325-00163-1
UCAC4	098-095039
Gaia	6375983988633147392
Equatorial coordinates	
RA (J2000.0)	$20^h49^m21^s.57$
Dec (J2000.0)	$-70^\circ29'05''.95$
Magnitudes	
TESS	11.3643 ± 0.0060
Johnson B	12.6740 ± 0.0160
Johnson V	11.9530 ± 0.0120
$G^{(a)}$	11.8175 ± 0.0002
$G_{\rm RP}{}^{(a)}$	11.3030 ± 0.0007
$G_{\rm BP}{}^{(a)}$	12.1712 ± 0.0014
g	12.2770 ± 0.0200
r	11.7500 ± 0.0150
i	11.6300 ± 0.0060
J	10.743 ± 0.024
H	10.452 ± 0.026
K	10.346 ± 0.023
WISE $W1$	10.326 ± 0.022
WISE $W2$	10.344 ± 0.019
Parallax$^{(a)}$ (mas)	3.7882 ± 0.0132
Systemic velocity$^{(a)}$ (km s^{-1})	35.51 ± 0.56
$\mu_{\rm RA}{}^{(a)}$ (mas yr^{-1})	16.326 ± 0.011
$\mu_{\rm Dec}{}^{(a)}$ (mas yr^{-1})	−20.168 ± 0.013
$T_{\rm eff}{}^{(b)}$ (K)	5634 ± 31
$M_\star{}^{(b)}$ ($M_\odot$)	1.032 ± 0.038
$R_\star{}^{(b)}$ ($R_\odot$)	1.043 ± 0.017
$\rho_*{}^{(b)}$ (g cm^{-3})	1.25 ± 0.09
$L_\star{}^{(b)}$ ($L_\odot$)	0.99 ± 0.04
$\log g_\star{}^{(b)}$	4.42 ± 0.04
[Fe/H]$^{(b)}$	0.14 ± 0.05
[Ca/H]$^{(b)}$	0.15 ± 0.06
[Mg/H]$^{(b)}$	0.18 ± 0.09
[Na/H]$^{(b)}$	0.20 ± 0.08
[Si/H]$^{(b)}$	0.15 ± 0.08
$V \sin i_\star{}^{(b)}$ (km s^{-1})	2.0 ± 0.4
Age$^{(b)}$ (Gyr)	4.5 ± 2.0

Notes. $^{(a)}$*Gaia* eDR3. $^{(b)}$This work (Sect. 3.2).

2. Observations

2.1. TESS photometry

Figure 1 shows a $3' \times 3'$ image from the Digitized Sky Survey 2 (DSS2) centered on TIC 372172128 (TOI-2196), marked with a cyan circle. TOI-2196 was observed by TESS[3] in sector 13,

[3] https://tess.mit.edu

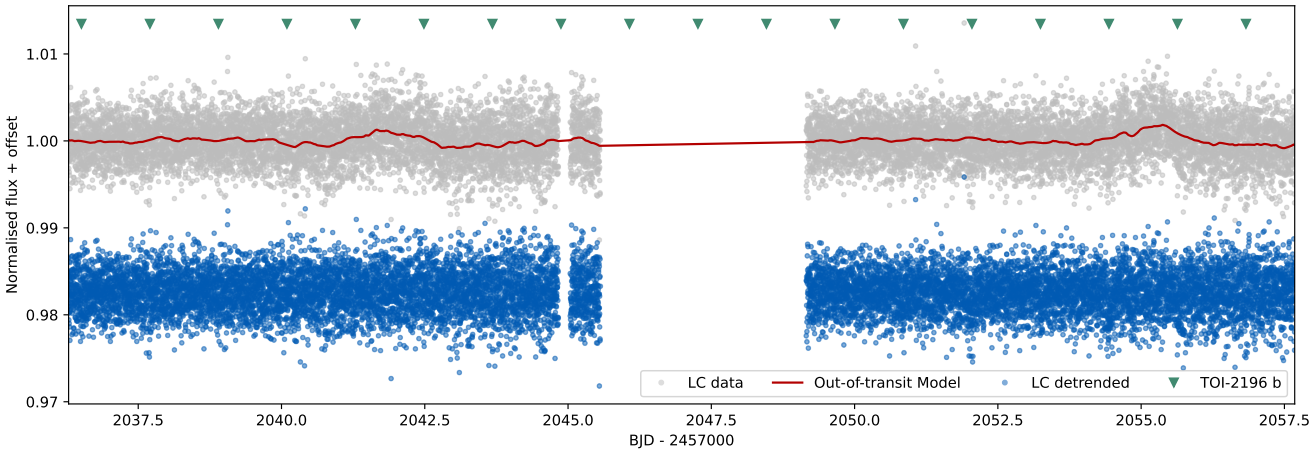

Fig. 2. TESS light curve for sector 27 (short cadence) is plotted in grey with the Gaussian Process model of the out-of-transit data overplotted in red. The detrended and normalised light curve is shown in blue, and, for the purposes of visualisation, a vertical offset has been applied. The triangles mark the locations of the individual transits of TOI-2196 b.

during the primary mission, and in sector 27 in the first set of observations of the TESS extended mission. The outline of the Science Processing Operations Center (SPOC) photometric aperture of sector 27 is overplotted in black in Fig. 1, while the red circles mark the positions of *Gaia* DR2 sources within 2′ from the target. The photometric dilution from other sources is negligible and adjusted for by the pipeline.

TOI-2196 was observed in sector 13 with camera 2 in full-frame images at a cadence of 30 min from 19 June to 17 July 2019. The observations of sector 27 spanned the interval 5 July through 30 July 2020, with a gap in the middle of approximately one day, when the data were being downloaded. This produced 23.35 days of science data at 2-min cadence, including 14 transits of TIC 372172128 monitored with camera 2, CCD 1.

Due to the combination of the short period of the planet (1.2 days) and the long cadence in sector 13, the planet candidate TOI-2196.01 was not discovered orbiting its G-type host star until it was observed in sector 27 at a 2-min cadence and processed by SPOC at NASA Ames Research Center (Jenkins et al. 2016). A search of the sector 27 data with an adaptive, wavelet-based matched filter (Jenkins 2002; Jenkins et al. 2010, 2020a) identified the transit signature of TOI-2196 b just above the detection threshold at 7.2 σ. The data validation reports (DVR; Twicken et al. 2018; Li et al. 2019) process fit a limb-darkened transit model with a signal-to-noise ratio (S/N) of 9.2, a period of 1.1954 days, a duration of 1.6 h, and a transit depth of 1127 ppm, corresponding to a preliminary planet radius of ~3.5 $R_{\oplus}$. We independently detected the transit signal using the DST (Cabrera et al. 2012) pipeline and found a planet candidate with an orbital period of 1.19387 ± 0.00043 days and a transit depth of 1359 ± 147 ppm.

We downloaded the light curves processed by the SPOC pipeline from the Mikulski Archive for Space Telescopes (MAST[4]) and used the Pre-search Data Conditioning Simple Aperture Photometry (PDCSAP) data. This was generated by the pipeline by identifying and correcting the SAP flux for instrumental signatures using cotrending basis vectors drawn from the light curves of an ensemble of quiet and highly temporally correlated stars long-term trends, thus resulting in a cleaner data set with fewer systematics (Stumpe et al. 2014; Jenkins et al. 2020a).

In order to remove any remaining low-frequency signals in preparation for the modelling described in Sect. 3.3, we further detrended the light curve by applying a Gaussian Process (GP). This was achieved using the package `citlalicue`[5] (e.g. Georgieva et al. 2021; Barragán et al. 2022a), a `PYTHON` wrapper of `george` (Foreman-Mackey et al. 2014) and `pytransit` (Parviainen 2015). We masked out the transits of the planet and applied a squared exponential covariance function as well as a 5 σ clipping algorithm to remove outliers. Figure 2 displays both the PDCSAP data in sector 27 with the GP model overplotted, and the detrended normalised light curve. The latter is subsequently used in the joint transit and RV analysis in Sect. 3.3.

2.2. Follow-up photometry from ground: LCOGT 1 m

The TESS pixel scale is ~21″ pixel^{-1} and photometric apertures typically extend out to roughly 1 arcmin. This generally results in multiple stars blending in the TESS aperture. An eclipsing binary in one of the nearby blended stars could mimic a transit-like event in the large TESS aperture. We therefore acquired ground-based transit follow-up photometry of TOI-2196 b as part of the TESS Follow-up Observing Program Sub Group 1 (TFOP SG1; Collins 2019)[6] to attempt to (1) rule out or identify nearby eclipsing binaries (NEBs) as potential sources of the detection in the TESS data; (2) check for the transit-like event on-target using smaller photometric apertures than TESS to confirm that the event is occurring on-target or, otherwise, in a star so close to TOI-2196 that it was not detectable by *Gaia* eDR3; (3) refine the TESS ephemeris; and (4) place constraints on transit depth across optical filter bands.

We observed the transits of TOI-2196 from the Las Cumbres Observatory Global Telescope (LCOGT; Brown et al. 2013) 1.0 m network on UTC 28 September 2020, 23 May 2021, and 6 June 2021 in Sloan i' band and on UTC 20 June 2021 in Sloan g' band. We used the `TESS Transit Finder` to schedule our transit observations. The 1.0 m telescopes are equipped with 4096 × 4096 SINISTRO cameras having an image scale of 0.″389 per pixel, resulting in a 26′ × 26′ field of view. The images were calibrated by the standard LCOGT `BANZAI` pipeline

[4] https://mast.stsci.edu/portal/Mashup/Clients/Mast/Portal.html

[5] https://github.com/oscaribv/citlalicue

[6] https://tess.mit.edu/followup

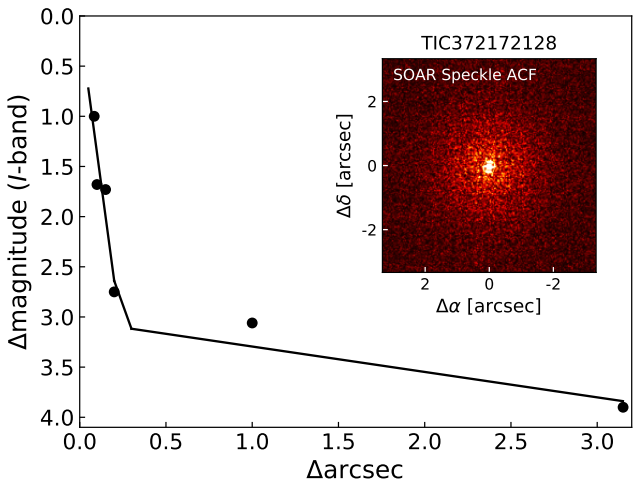

Fig. 3. Contrast curve computed from observations in Cousins I-band on the 4.1 m Southern Astrophysical Research telescope. No bright companions are detected within 3″ of TOI-2196.

(McCully et al. 2018). Photometric data were extracted using `AstroImageJ` (Collins et al. 2017) and circular photometric apertures with radii in the range 4.″7 to 7.″0. The TOI-2196 apertures exclude virtually all flux from the nearest *Gaia* eDR3 and TESS Input Catalog neighbor (TIC 1988186200) 12.″5 South. We find no evidence for an NEB within 2.′5 of TOI-2196, and detect the transit event within the TOI-2196 photometric apertures.

2.3. Follow-up speckle imaging from ground

High-angular resolution imaging is needed to search for nearby sources that can contaminate the TESS photometry. This can result in an underestimated planetary radius or may be the source of astrophysical false positives such as background eclipsing binaries. We searched for stellar companions to TOI-2196 with speckle imaging on the 4.1 m Southern Astrophysical Research (SOAR) telescope (Tokovinin 2018) on 31 October 2020, observing in Cousins I-band, a visible bandpass similar to that of TESS. This observation was sensitive to a 3 magnitude fainter star at an angular distance of 1″ from the target. More details of the observation are available in Ziegler et al. (2020). The 5 σ detection sensitivity and speckle auto-correlation functions from the observations are shown in Fig. 3. No nearby stars were detected within 3″ of TOI-2196 in the SOAR observations.

2.4. Radial velocity follow-up with HARPS

We performed high-resolution ($R \approx 115\,000$) spectroscopic observations of TOI-2196 using the High Accuracy Radial velocity Planet Searcher (HARPS; Mayor et al. 2003) spectrograph mounted at the ESO 3.6 m telescope (La Silla observatory, Chile). We obtained a total of 41 spectra between 24 July 2021 and 12 November 2021 UT as part of our HARPS large program (ID: 106.21TJ.001, PI: Gandolfi). All RVs and activity indicators are listed in Table A.1 along with $\mathrm{BJD_{TBD}}$, exposure time, and S/N. We reduced the data with the dedicated HARPS data reduction software (DRS) available at the observatory (Lovis & Pepe 2007) and extracted the radial velocity (RV) measurements using the code HARPS-TERRA (Anglada-Escudé & Butler 2012), which employs a template-matching algorithm to derive precise relative velocities. We also extracted a variety of stellar activity and line profile variation indicators: the Hα and S-index were

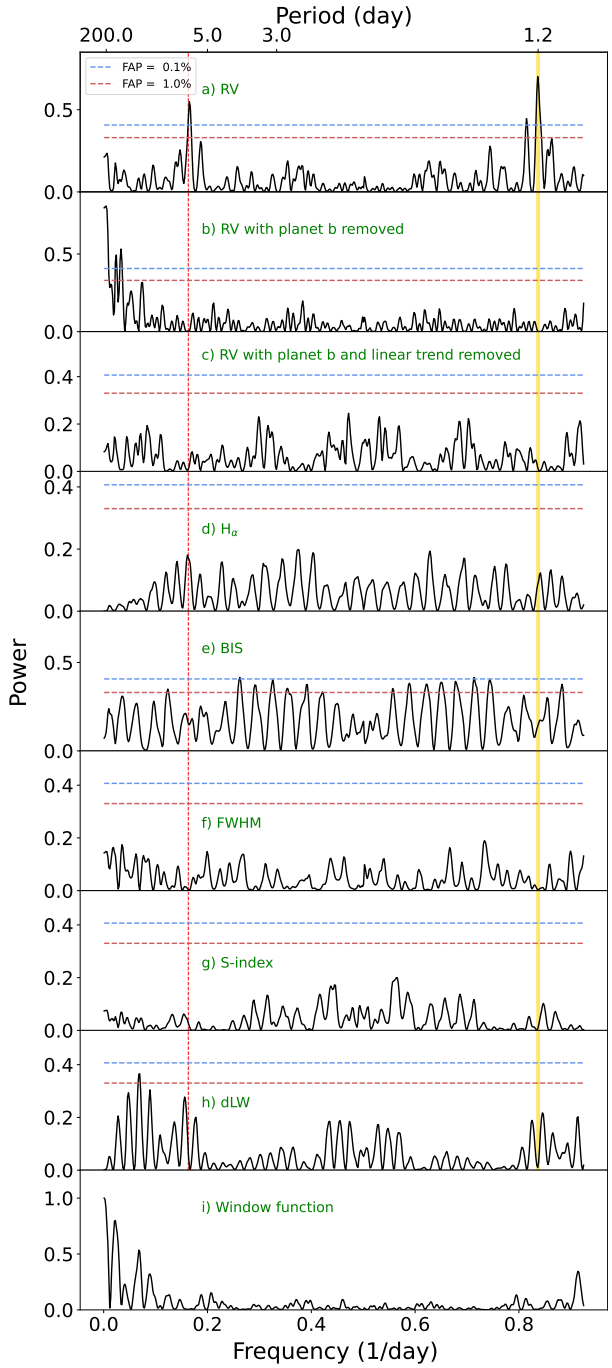

Fig. 4. Generalised Lomb–Scargle periodogram of the HARPS RVs and stellar activity indicators. The horizontal lines mark the bootstrap false alarm probabilities at 0.1 and 1.0% as indicated in the legend. The orbital frequency of TOI-2196 b ($\nu_{\rm b} = 0.837$ day^{-1}) is marked with a vertical thick yellow line, while the corresponding period is reported in the upper x-axis ($P_{\rm orb} \approx 1.2$ day). The 1 day alias of planet b is marked with a vertical dashed red line ($1 - 0.837 = 0.163$ day^{-1}). *a)* RV measurements. *b)* RV residuals with the best-fitting Keplerian orbit of planet b subtracted. *c)* RV residuals following the subtraction of both the linear trend and the Doppler signal induced by planet b. *d–h)* Activity indicators and line profile variations. *i)* The window function.

extracted using TERRA; the FWHM and the bisector inverse slope (BIS) were derived by cross-correlating the HARPS spectra with a G2 numerical mask (Baranne et al. 1996; Pepe et al. 2002); and the differential line width (dLW) was extracted using the code SERVAL (Zechmeister et al. 2018).

Table 2. Spectroscopic parameters for TOI-2196 modelled with `SME` and `SpecMatch-Emp`, posteriors from the `ARIADNE`, and the effective stellar temperature from *Gaia* DR2.

Method	$T_{\rm eff}$ (K)	log(g) (dex)	[Fe/H] (cgs)	[Ca/H] (km s^{-1})	[Mg/H]	[Na/H]	[Si/H]	$V \sin i_\star$
`SME`[(a)]	5552 ± 85	4.42 ± 0.05	0.14 ± 0.05	0.15 ± 0.06	0.18 ± 0.09	0.20 ± 0.08	0.15 ± 0.08	2.0 ± 0.4
`SpecMatch-Emp`	5623 ± 110	4.22 ± 0.12	0.18 ± 0.09	...	...	...	...	...
`ARIADNE`[(b)]	5634 ± 31	4.42 ± 0.04	0.13 ± 0.05	...	...	...	...	...
Gaia DR2	5462^{+176}_{-66}	...	...	...	...	...	...	...

Notes. [(a)]Adopted as priors for the stellar mass and radius modelling in Sect. 3.2. [(b)]Posteriors from Bayesian Model Averaging with ARIADNE.

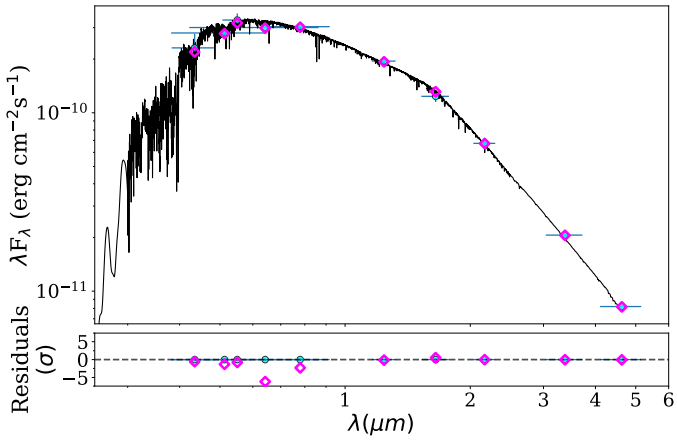

Fig. 5. Spectral energy distribution (SED) of TOI-2196 and the model with highest probability from Husser et al. (2013, `Phoenix v2`). We plot the synthetic photometry with magenta diamonds and the observed photometry with blue points. The 1 σ uncertainties are shown with vertical error bars, while the horizontal bars display the effective width of the passbands. In the *lower panel* we show the residuals normalised to the errors of the photometry.

3. Data analysis

3.1. Frequency analysis of HARPS data

In order to search for the Doppler reflex motion induced by the transiting planet and unveil the presence of additional RV signals, we performed a frequency analysis of the HARPS RV measurements and activity indicators. To this aim, we computed the generalised Lomb-Scargle (GLS; Zechmeister & Kürster 2009) periodograms of the HARPS time series (shown in Fig. 4) and estimated the false alarm probabilities (FAPs) using the bootstrap technique described in Kuerster et al. (1997). We considered a peak to be significant if its FAP is less than 0.1%.

The GLS periodogram of the HARPS RVs displays a significant peak at $\nu_{\rm b}$ = 0.837 day^{-1} which is the transit frequency of TOI-2196 b (Fig. 4, upper panel, thick vertical yellow line). This peak is not significantly detected in any of the activity indicators confirming the planetary nature of the transit signal found in the TESS light curve. We note the presence of a second significant peak at 0.163 day^{-1} (vertical dashed red line), which is an alias of the orbital frequency of the transiting planet due to the 1 day sampling of our observations.

The second panel of Fig. 4 displays the periodogram of the HARPS RV residuals following the subtraction of the best-fitting Doppler orbit of TOI-2196 b (Sect. 3.3). We found a significant excess of power at frequencies lower than the frequency resolution of our observations (≈1/110 day = 0.009 day^{-1}, where 110 days is the baseline of our observations). This power has no counterpart in any of the activity indicators, suggesting that it is likely caused by an outer orbiting companion. As described in Sect. 3.3, we accounted for this long-period Doppler signal by adding a linear trend to the RV model. When both the Doppler signal of the transiting planet and the linear trend are subtracted from the HARPS RVs, no additional significant signals are found in the RV residuals (Fig. 4, third panel).

3.2. Stellar properties

In order to derive the fundamental parameters of the host star, we analysed our co-added high-resolution HARPS spectra with two methods, the `SpecMatch-Emp` code (Yee et al. 2017) and `SME`[7] (Spectroscopy Made Easy; Valenti & Piskunov 1996; Piskunov & Valenti 2017). In particular, `SpecMatch-Emp` is an empirical code that compares observations of optical spectra to a dense library of well-characterised FGKM stars, while `SME` fits observed spectra to computed synthetic spectra for a chosen set of parameters based on atomic and molecular line data from VALD[8] (Ryabchikova et al. 2015) and a stellar atmosphere grid. We chose Atlas12 (Kurucz 2013) and derived the stellar effective temperature, $T_{\rm eff}$, the surface gravity, $\log g_\star$, abundances, and the projected rotational velocity, $V \sin i_\star$. Each parameter is modelled, one at a time, from specific spectral lines: the broad line wings of H$_\alpha$ are particularly sensitive to $T_{\rm eff}$, and the line wings of the Ca I triplet 6102, 6122, and 6162 Å are sensitive to the surface gravity. Abundances and the projected stellar rotational velocity, $V \sin i_\star$, were modelled from narrow and unblended lines between 6000 and 6600 Å. We held the micro- (Bruntt et al. 2008) and macro-turbulent (Doyle et al. 2014) velocities fixed to 1.0 km s^{-1}, and 2.8 km s^{-1}, respectively. Further details on the modelling can be found in Fridlund et al. (2017) and Persson et al. (2018). Results from both models listed in Table 2 are in good agreement within the uncertainties and with the effective temperature from *Gaia*[9] DR2.

We used the spectral parameters from `SME` as priors to model the stellar radius and mass with the python code `ARIADNE`[10] (Vines & Jenkins 2022). We fit the broadband photometry bandpasses $GG_{\rm BP}G_{\rm RP}$ from *Gaia* eDR3 and WISE W1–W2, along with JHK$_{\rm S}$ magnitudes from *2MASS*, the Johnson B and V magnitudes from APASS, and the *Gaia* eDR3 parallax, to the `Phoenix v2` (Husser et al. 2013), `BtSettl` (Allard et al. 2012), Castelli & Kurucz (2004), and Kurucz (1993) atmospheric

[7] http://www.stsci.edu/~valenti/sme.html
[8] http://vald.astro.uu.se
[9] https://gea.esac.esa.int/archive/
[10] https://github.com/jvines/astroARIADNE

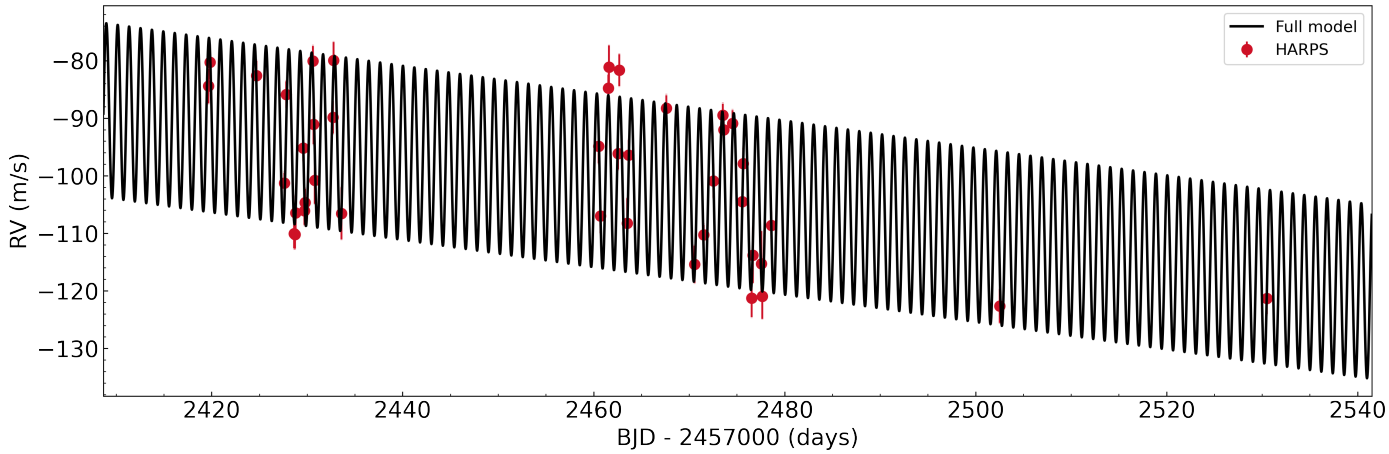

Fig. 6. Radial velocity times series of TOI-2196 and the best-fitting RV model. The linear trend suggesting the presence of an outer companion is clearly identifiable.

model grids. The dust maps of Schlegel et al. (1998) were used to obtain an upper limit on A_V. The relative probabilities of the models were used to compute a weighted average of each parameter and the final stellar radius is computed with Bayesian model averaging. Figure 5 shows the SED model and the fitted bands. The `Phoenix v2` model, which has the highest probability, was used to calculate the synthetic photometry. We also obtained a luminosity of $0.99 \pm 0.04\ L_\odot$, an extinction that is consistent with zero ($A_V = 0.03 \pm 0.02$), as well as the stellar mass based on MIST (Choi et al. 2016) isochrones. The model was checked with `BASTA`[11] (the BAyesian STellar Algorithm; Aguirre Børsen-Koch et al. 2022) using the stellar atmosphere grid from Hidalgo et al. (2018) and the same photometry passbands and priors as above, as well as `PARAM1.3`[12] (da Silva et al. 2006). The latter model uses Bayesian computation of stellar parameters based on PARSEC isochrones using V magnitude, $T_{\rm eff}$, [Fe/H], and the *Gaia* eDR3 parallax as priors.

The results, listed in Table 3, are in excellent agreement within the 1 σ uncertainties. We adopted the stellar parameters derived with `ARIADNE` in our joint modelling of the radial velocities and light curves in Sect. 3.3.

The stellar age was estimated with the observed NUV excess utilising empirical activity–age relations. We transformed the NUV and $B-V$ photometry to $\log R'_{\rm HK} = -4.92 \pm 0.08$ via the empirical relations of Findeisen et al. (2011), which implies an age of $\tau_\star = 5.2 \pm 1.3$ Gyr, according to the empirical relations of Mamajek & Hillenbrand (2008). This is in agreement with 4.5 ± 2.0 Gyr and 7.1 ± 3.4 Gyr derived from the MIST and PARSEC isochrones, respectively, in the above modelling. We note that there is no emission in the Ca I H and K lines, suggesting that the star is not chromospherically active.

3.3. Joint transit and radial velocity modelling

For the modelling of the TOI-2196 system, we turned to the open-source code `pyaneti`[13] (Barragán et al. 2019b, 2022a) to sample the parameter space using Markov chain Monte Carlo (MCMC) sampling combined with a Bayesian approach. Following Barragán et al. (2022b), we used `pyaneti`'s capability to perform multi-band fits and included the flattened TESS light curve (Sect. 2.1), the LCOGT light curves (Sect. 2.2), and the RVs listed in Table A.1 in our joint model.

The parametrisation of the limb darkening coefficients q_1 and q_2 was handled as per Kipping (2013), while the limb darkening model followed the quadratic approach by Mandel & Agol (2002). We placed a loose informative prior on the scaled semi-major axis, as well as on q_1 and q_2, based on the tables by Claret (2017) for the TESS band, and Claret et al. (2013) for the ground-based photometry. For the remaining parameters, we used uniform priors. We tested a model in putting a beta prior on the eccentricity of the planet and find an eccentricity consistent with zero. Given the short period of the planet, we thus assumed a circular orbit and sampled the parameter space using 250 independent chains thinned with a factor of ten and created posterior distributions with the last 5000 iterations. This translates to 125 000 points for each sampled parameter per distribution.

We first carried out a sampling for the independent scaled planet radii ($R_p/R_\star$) for the TESS and each of the LCOGT bands. We obtain values of $R_{\rm SAAO} = 3.37^{+0.36}_{-0.57}\ R_\oplus$, $R_{\rm CTIO} = 3.42^{+0.58}_{-0.36}\ R_\oplus$, $R_{\rm SSO} = 3.34 \pm 0.37\ R_\oplus$, and $R_{\rm TESS} = 3.61 \pm 0.26\ R_\oplus$ individually, thus demonstrating independent detections from each facility and full consistency (within 1 σ) between the different estimates. We thereby assumed the same transit depth for each band for our final model.

The RV times series with the best-fitting RV model is shown in Fig. 6, which clearly displays a linear trend in the RVs pointing toward the presence of an outer companion (see Sect. 3.4). The model containing the linear trend is significantly favoured over the one with no trend (ΔBIC = 54). The RVs folded to the orbital period of the planet are shown in Fig. 7 with the RV model and

Table 3. Comparison of models of the stellar mass and radius.

Method	$M_\star$ ($M_\odot$)	$R_\star$ ($R_\odot$)	$\rho_\star$ (g cm^{-3})
`ARIADNE`[(a)]	1.032 ± 0.038	1.043 ± 0.017	1.25 ± 0.09
Gravitational mass	1.0 ± 0.1	...	...
`BASTA`	0.973 ± 0.053	1.045 ± 0.025	1.20 ± 0.11
`PARAM 1.3`	0.982 ± 0.037	1.049 ± 0.034	1.23 ± 0.14
Gaia DR2	...	$1.103^{+0.027}_{-0.068}$	...

Notes. [(a)]Adopted for the modelling in Sect. 3.3.

[11] https://github.com/timkahlke/BASTA
[12] http://stev.oapd.inaf.it/cgi-bin/param_1.3
[13] https://github.com/oscaribv/pyaneti

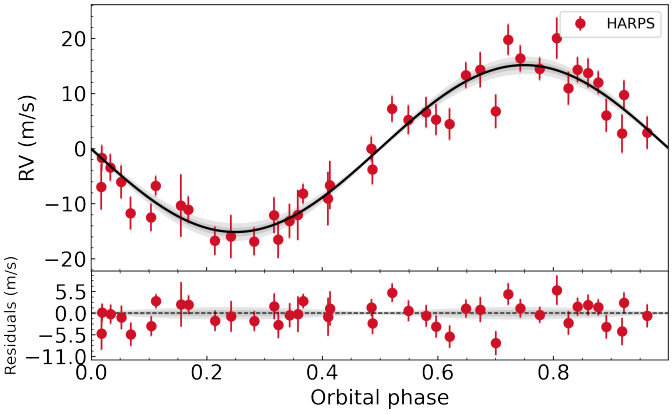

Fig. 7. HARPS radial velocity data phase-folded on the orbital period of TOI-2196 b after subtraction of the stellar systemic velocity and the linear trend. The solid black line is the RV model with 1 σ and 2 σ credible intervals in shaded grey areas.

1 σ and 2 σ credible intervals in shaded grey areas. The four light curves of TOI-2196 b are shown in Fig. 8, together with the best-fit transit model with a single radius plotted in solid black in each panel.

All results and priors are listed in Table 4 along with the adopted stellar parameters derived in Sect. 3.2 used in the modelling. All adopted stellar parameters are also listed in Table 1.

3.4. Evidence of an outer companion

The assumption of a long-period companion is supported by the periodogram (panel 2 in Fig. 4) and the linear trend in the RV data (Table 4 and Fig. 6). We computed the minimum mass of this outer companion, here denoted with c, using the measured linear trend of -0.238 ± 0.019 m s^{-1} day^{-1} from our RV analysis in Sect. 3.3 and Eq. (2) of Bowler (2016):

$$\frac{M_c}{a_c^2} > 0.0145 \left| \frac{\dot{\gamma}}{\mathrm{m\ s^{-1}\ yr^{-1}}} \right| = 1.3\ M_J\ \mathrm{au}^{-2}, \quad (1)$$

where $\dot{\gamma}$ is the slope of the linear trend (acceleration), and a_c is the minimum semi-major axis compatible with the RV data. Following Smith et al. (2017), we assumed zero eccentricity and a minimum orbital period of twice the baseline of our RV measurements ($P_{\mathrm{orb,c}} > 222$ days), resulting in a minimum semi-major axis of 0.717 ± 0.009 au and a corresponding minimum mass of $0.65 \pm 0.05\ M_J$.

We note that the *Gaia* renormalised unit weight error (RUWE) value[14] is 0.99 for TOI-2196, corresponding to a low astrometric signal. This implies that a low-mass stellar companion scenario is unlikely. However, future long-term RV monitoring of the star is needed to firmly determine the nature of the signal.

4. Discussion

4.1. The hot Neptune desert

TOI-2196 b is one of very few planets found in the hot Neptune desert (shown in Fig. 9). In this figure, we plot in grey

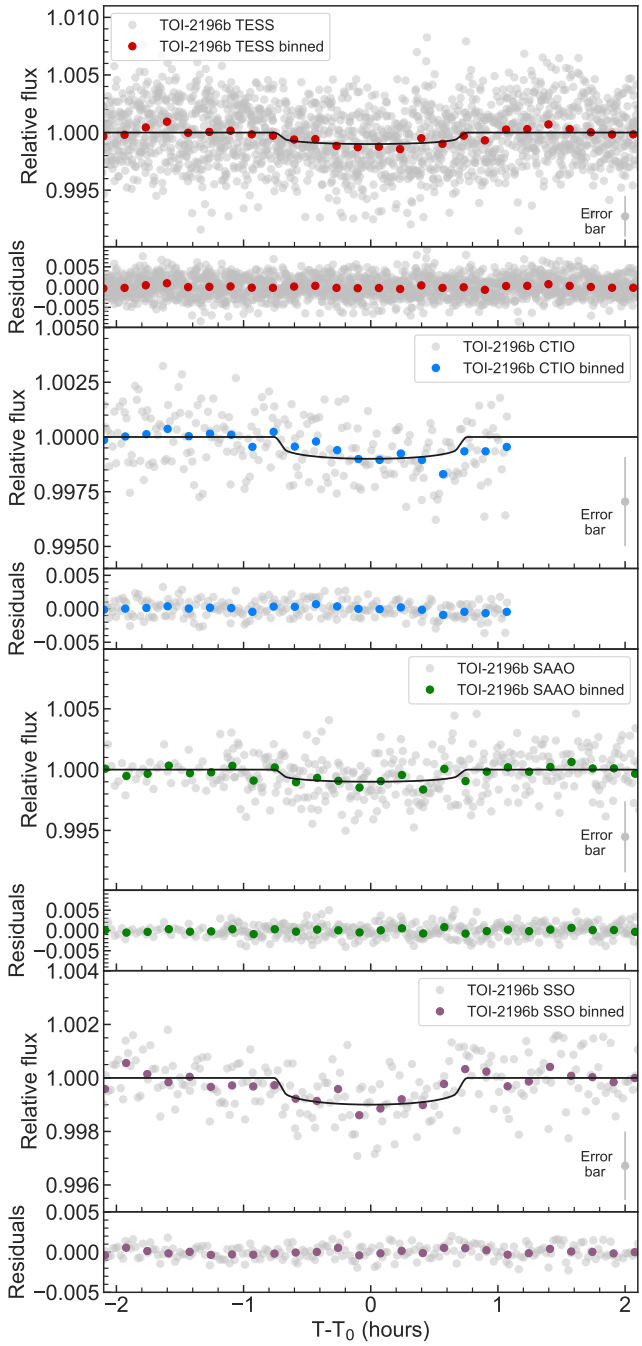

Fig. 8. Flattened and phase-folded TESS light curve with the best-fitting transit model in black in the *top panel*, and follow-up photometry from ground performed with the LCOGT CTIO, SAAO, and SSO telescopes in the *second to fourth panels* as marked in the legends. The CTIO and SSO panels show the single transits those facilities observed, while the SAAO panel shows the two stacked transits detected with that telescope. The nominal short cadence data are plotted in grey in all panels and binned to 10 min in colour.

the radius of all known planets with radius measurements from transit surveys with a precision of 10% or better as a function of equilibrium temperature. About a third of the planets in Fig. 9 also have masses from RV measurements with a precision of 30% or better and are colour-coded with mass. The data were downloaded from the NASA Exoplanet archive[15] and

[14] https://gea.esac.esa.int/archive/documentation/GDR2/Gaia_archive/chap_datamodel/sec_dm_main_tables/ssec_dm_ruwe.html

[15] https://exoplanetarchive.ipac.caltech.edu

Table 4. Description of the `pyaneti` model of TOI-2196 b from Sect. 3.3 and the adopted stellar parameters used in the model from Sect. 3.2.

Parameter	Units	Priors [(a)]	Final value
Stellar parameters			
$M_\star$	Stellar mass ($M_\odot$)	$\mathcal{F}[1.032]$	1.032 ± 0.038
$R_\star$	Stellar radius ($R_\odot$)	$\mathcal{F}[1.043]$	1.043 ± 0.017
$T_{\rm eff}$	Effective temperature (K)	$\mathcal{F}[5634]$	5634 ± 31
Fitted parameters			
T_0	Transit epoch ($\rm BJD_{TDB}$ - 2 457 000)	$\mathcal{U}[2036.4888, 2036.5288]$	$2036.5126^{+0.0019}_{-0.0016}$
$P_{\rm orb}$	Orbital period (days)	$\mathcal{U}[1.1943, 1.1963]$	$1.1947268^{+7.9e-06}_{-9.3e-06}$
e	Eccentricity	$\mathcal{F}[0]$	0
ω	Argument of periastron (degrees)	$\mathcal{F}[90]$	90
b	Impact parameter	$\mathcal{U}[0, 1]$	$0.712^{+0.034}_{-0.036}$
$a/R_\star$	Scaled semi-major axis	$\mathcal{N}[4.6, 0.1]$	4.61 ± 0.10
$R_{\rm p}/R_\star$	Scaled planet radius	$\mathcal{U}[0.01, 0.10]$	$0.0308^{+0.0013}_{-0.0012}$
K	Doppler semi-amplitude variation (m s^{-1})	$\mathcal{U}[0, 50]$	$15.16^{+0.67}_{-0.69}$
q_1	Limb-darkening coefficient, TESS	$\mathcal{N}[0.26, 0.10]$	0.27 ± 0.10
q_2	Limb-darkening coefficient, TESS	$\mathcal{N}[0.47, 0.10]$	0.47 ± 0.10
q_1	Limb-darkening coefficient, LCOGT CTIO	$\mathcal{N}[0.52, 0.10]$	0.51 ± 0.10
q_2	Limb-darkening coefficient, LCOGT CTIO	$\mathcal{N}[0.17, 0.10]$	0.18 ± 0.09
q_1	Limb-darkening coefficient, LCOGT SSO	$\mathcal{N}[0.52, 0.10]$	0.54 ± 0.10
q_2	Limb-darkening coefficient, LCOGT SSO	$\mathcal{N}[0.17, 0.10]$	0.18 ± 0.09
q_1	Limb-darkening coefficient, LCOGT SAAO	$\mathcal{N}[0.52, 0.10]$	0.53 ± 0.10
q_2	Limb-darkening coefficient, LCOGT SAAO	$\mathcal{N}[0.17, 0.10]$	0.17 ± 0.10
Derived parameters			
$M_{\rm b}$	Planet mass ($M_\oplus$)	...	26.0 ± 1.3
$R_{\rm b}$	Planet radius ($R_\oplus$)	...	3.51 ± 0.15
i [(b)]	Inclination (degrees)	...	$81.11^{+0.57}_{-0.55}$
a	Semi-major axis (au)	...	0.02234 ± 0.00060
F	Instellation ($F_\oplus$)	...	2000 ± 100
$\rho_{\rm b}$	Planet density (g cm^{-3})	...	$3.31^{+0.51}_{-0.43}$
$g_{\rm b}$	Planet surface gravity (cm s^{-2})	...	2100 ± 200
$T_{\rm eq}$ [(c)]	Equilibrium temperature (K)	...	1860 ± 20
Λ [(d)]	Jeans escape parameter	...	30 ± 2
TSM[(e)]	Transmission spectroscopy metric	...	$25.8^{+3.6}_{-3.3}$
T_{14}	Total transit duration (h)	...	$1.504^{+0.054}_{-0.059}$
T_{23}	Full transit duration (h)	...	$1.325^{+0.065}_{-0.072}$
T_{12}	Ingress and egress transit duration (h)	...	$0.0892^{+0.0087}_{-0.0076}$
Additional parameters			
$\dot{\gamma}_1$	Linear trend HARPS (m s^{-1} days^{-1})	$\mathcal{U}[-100, 100]$	-0.238 ± 0.019
$\dot{\gamma}_1$	Systemic velocity HARPS (km s^{-1})	$\mathcal{U}[-1.0218, 1.0208]$	0.1008 ± 0.0079
σ_{F1}	RV jitter HARPS (m s^{-1})	$\mathcal{J}[10^{-3}, 10^{-1}]$	$1.2^{+0.77}_{-0.80}$
$\sigma_{\rm TESS}$	TESS light curve jitter	$\mathcal{J}[10^{-2}, 10^{-3}]$	$0.002433 \pm 1.7e-05$
$\sigma_{\rm CTIO}$	LCOGT CTIO light curve jitter	$\mathcal{J}[10^{-2}, 10^{-3}]$	$0.001376^{+5.1e-05}_{-4.8e-05}$
$\sigma_{\rm SSO}$	LCOGT SSO light curve jitter	$\mathcal{J}[10^{-2}, 10^{-3}]$	$0.000939^{+3.9e-05}_{-3.7e-05}$
$\sigma_{\rm SAAO}$	LCOGT SAAO light curve jitter	$\mathcal{J}[10^{-2}, 10^{-3}]$	$0.001706^{+5.4e-05}_{-5.0e-05}$

Notes. [(a)]$\mathcal{U}[a, b]$ refers to uniform priors in the range a– b, $\mathcal{F}[a]$ to a fixed value a, $\mathcal{N}[a, b]$ to Gaussian priors with mean a and standard deviation b, and $\mathcal{J}[a, b]$ to modified Jeffrey's priors (Eq. (16) in Gregory 2005). [(b)]Orbit inclination relative to the plane of the sky. [(c)]Dayside equilibrium temperature, assuming no heat redistribution and zero albedo (Eq. (2)). [(d)]Jeans escape parameter defined as $\Lambda = GM_{\rm p}m_{\rm H}/(k_{\rm B}T_{\rm eq}R_{\rm p})$ in Fossati et al. (2017). [(e)]Kempton et al. (2018).

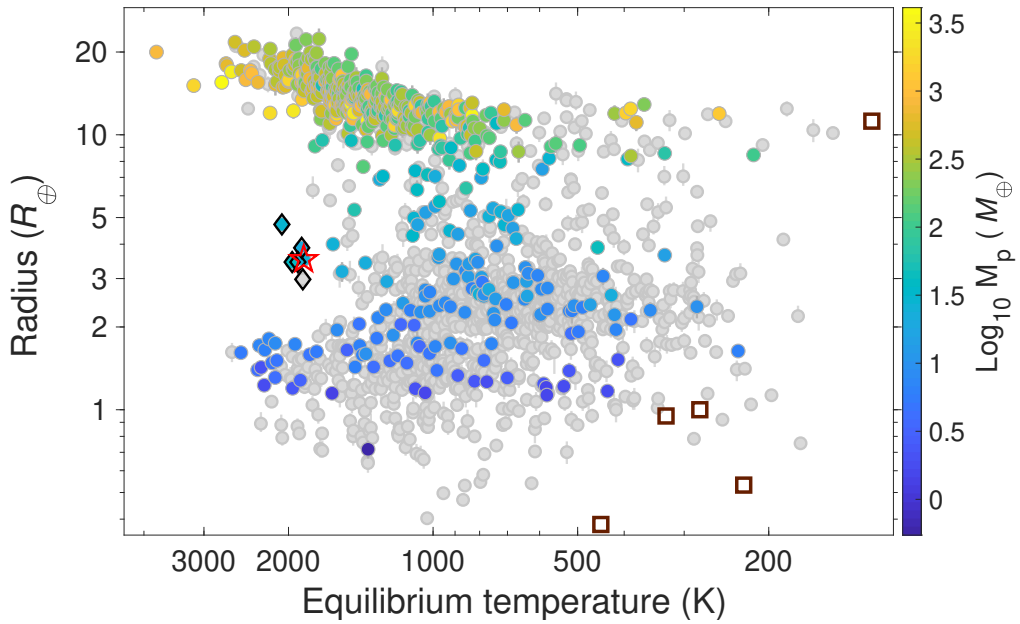

Fig. 9. Radius vs. equilibrium temperature diagram: known planets with a precision of 10% or better in radius are plotted in grey. About a third of these planets have also RV mass measurements with a precision of 30% or better and are colour-coded with planet mass. We set upper limits to planet masses at 13 M_J. TOI-2196 b is marked with a red star symbol, the five additional planets in the hot Neptune desert with black diamonds, and solar system planets with brown squares. The five additional planets located in the desert are: K2-100 b (Barragán et al. 2019a), TOI-849 b (Armstrong et al. 2020), LTT 9779 b (Jenkins et al. 2020b), K2-278 b (Livingston et al. 2018), and Kepler-644 b (Berger et al. 2018) of which the latter two have only radius measurements.

Table 5. Known sub-Neptune and Neptune planets in the hot Neptune desert (T_{eq} > 1800 K) with a precision in radius of 10% or better. In addition to TOI-2196 b, three of the planets have RV measurements with a precision of 30% or better.

Planet	Radius ($R_\oplus$)	Mass ($M_\oplus$)	Bulk density (g cm^{-3})	P_{orb} (days)	T_{eq} (K)	T_{eff} (K)	[Fe/H]	Λ [a]	Age (Gyr)	Ref.
TOI-2196 b	3.51 ± 0.15	26.0 ± 1.3	$3.31^{+0.51}_{-0.43}$	1.20	1860	5634	0.14 ± 0.05	29.6	4.5 ± 2.0	(b)
K2-278 b	2.98 ± 0.23	...	...	3.33	1867	6747	0.00 ± 0.17	...	...	(c)
K2-100 b	3.88 ± 0.16	21.8 ± 6.2	2.05 ± 0.64	1.67	1878	5945	0.22 ± 0.09	22.8	$0.75^{+0.004}_{-0.007}$	(d)
TOI-849 b	$3.44^{+0.16}_{-0.12}$	39.1 ± 2.6	5.26 ± 0.71	0.77	1966	5374	0.19 ± 0.03	43.9	$6.7^{+2.8}_{-2.4}$	(e)
Kepler-644 b	$3.44^{+0.18}_{-0.35}$	...	...	3.17	1912	6540	0.08 ± 0.15	...	$1.6^{+0.52}_{-0.32}$	(f)
LTT 9779 b	4.72 ± 0.23	29.3 ± 0.8	1.53 ± 0.23	0.79	2064	5443	0.27 ± 0.03	22.9	$1.9^{+1.7}_{-1.2}$	(g)

References. [a]Fossati et al. (2017). [b]This work. [c]Livingston et al. (2018). [d]Barragán et al. (2019a). [e]Armstrong et al. (2020). [f]Berger et al. (2018). [g]Jenkins et al. (2020b).

we chose the latest results with the highest precision for planets with several entries or, if they share a similar precision, we chose the most recent results. Since the information about equilibrium temperature is not always given by the references, we computed T_{eq} in the same way for all planets with (e.g. Charbonneau et al. 2005):

$$T_{eq} = \sqrt{\frac{R_\star}{2\,a}}\, T_{eff}\, [f\,(1 - A_B)]^{1/4}, \tag{2}$$

where a is the planet's semi-major axis (computed with Kepler III), A_B is the Bond albedo, and f is the heat redistribution factor. The latter two parameters are here assumed to be zero and unity, respectively. We prefer to use T_{eq} over orbital period since the latter does not take into account differences of stellar types which may give misleading results. With fixed Bond albedo and heat redistribution, an ultra-short period planet with P_{orb} < 1 day around an M-dwarf has a lower equilibrium temperature than a planet with an orbital period of several days orbiting a sun-like star.

The dearth of short-period Neptunes is clearly seen in Fig. 9. In this plot, the desert starts around 1600 K for medium-sized planets, which corresponds to orbital periods of 1.9 days around sun-like stars. For equilibrium temperatures higher than 1800 K, most planets have $R_p \lesssim 1.8\ R_\oplus$ or $R_p \gtrsim 1\ R_J$. In addition to TOI-2196 b, we identified five more planets confirmed in the desert, which are listed in Table 5: K2-100 b (Barragán et al. 2019a), TOI-849 b (Armstrong et al. 2020), LTT 9779 b (Jenkins et al. 2020b), K2-278 b (Livingston et al. 2018), and Kepler-644 b (Berger et al. 2018) of which the latter two have no mass measurements. This diagram suggests that this small group of planets delimits two regimes: a hot sub-Neptune desert for planets with radii between 1.8 and 3 $R_\oplus$, and a sub-Jovian desert for radii 5–12 $R_\oplus$. More planets in this parameter space are needed

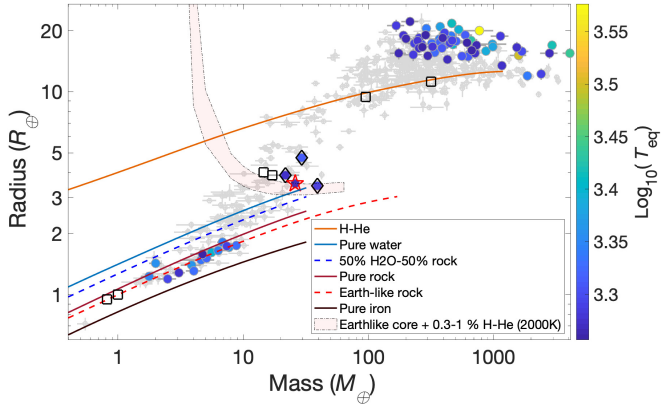

Fig. 10. Diagram of all known planets with masses from radial velocity measurements up to 13 M_J and radii from transit photometry with 30% and 10% uncertainties or lower in mass and radius, respectively. Planets with $T_{eq} \geq 1800$ K are colour-coded with T_{eq}, and the rest are plotted in light grey. In total, there are four planets (including TOI-2196 b) with radii between 3 and 5 $R_\oplus$ in this diagram that are identified as hot Neptune desert planets (cf. Fig. 9). TOI-2196 b is marked with a red star symbol and the three additional planets with black diamonds. Solar system planets are marked with brown squares. Interior models from Zeng et al. (2019) are plotted as listed in the legend. The 100% water line is for a planet with condensed water phases.

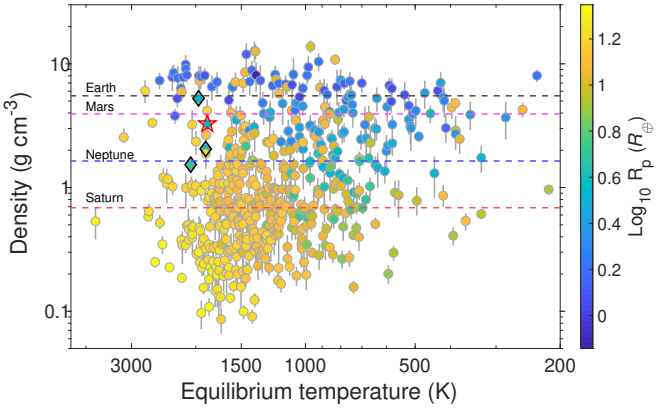

Fig. 11. Bulk density-equilibrium temperature diagram of the same planets as in Fig. 10 colour-coded here with planet radius. The densities of Earth, Mars, Neptune, and Saturn are marked with dashed-coloured lines.

to establish whether this is a selection effect or some kind of stability island in the desert.

In Fig. 10, we show the position of TOI-2196 b in a mass–radius diagram. We plot the same planets with both radii and RV masses as plotted in Fig. 9. Here, all planets are plotted in grey except for planets with $T_{eq} \geq 1800$ K which are colour-coded with equilibrium temperature. TOI-2196 b has a radius smaller than Neptune but an approximately 50% higher mass and, hence, twice Neptune's density. As already noted in Fig. 9, it joins the small group of the three planets found between small, rocky planets and gaseous giants. We also plot interior structure models from Zeng et al. (2019)[16] with and without the addition of atmospheres as listed in the legend. According to these models, the composition of TOI-2196 b is consistent with an Earth-like core with an 0.3–1% H-He atmosphere at an equilibrium temperature of 2000 K, and also lies slightly above a pure (condensed) water planet model. We investigated the atmospheric loss and interior composition with a model that considers water or H/He phases for highly-irradiated planets such as TOI-2196 b in Sects. 4.2 and 4.3, respectively.

To allow for a comparison to both previous plots, we plotted planet bulk densities versus equilibrium temperatures in Fig. 11, colour-coded according to planetary radius. The hot Neptune desert is also visible in this plot, albeit less prominent since planets with $\gtrsim 1$ M_J have increasingly higher densities, thereby filling in the lower parts of the $\rho - T_{eq}$ desert. Most planets in this plot with high T_{eq} have either high densities or large radii if the densities are low.

To investigate any potential correlations with stellar metallicity, we plotted the radius versus the iron abundance relative to hydrogen in Fig. 12. In panel a) we plot all planets and in panel b) we plot planets with $T_{eq} \geq 1800$ K. We note that all hot Neptune desert planets have greater than solar iron abundances, although the sample is too small to draw any firm conclusions.

[16] https://lweb.cfa.harvard.edu/~lzeng/planetmodels.html

4.2. Atmospheric loss

Planets in close proximity to their host stars are exposed to high levels of X-ray and extreme UV radiation (XUV) that can erode planetary atmospheres. If the escape is energy limited, the atmospheric mass loss rate of TOI-2196 b can be written as (Erkaev et al. 2007; Owen & Wu 2013):

$$\dot{M} = \epsilon \frac{\pi F_{XUV} R_p^3}{G M_p}, \tag{3}$$

where F_{XUV} is the XUV flux received by the planet, G the gravitational constant, and ϵ is an efficiency parameter. Planets with low densities in close orbits are most susceptible to mass loss, with ϵ that can also depend on the mass and radius of the planet (Owen & Jackson 2012). Since the mass of the atmosphere of average sub-Neptunes is typically 1−10% of the planetary mass (Lopez & Fortney 2014), atmospheric loss is possible and can transform the planet into a rocky super-Earth (Lopez & Fortney 2013; Owen & Wu 2013).

The XUV irradiation produced by solar-type stars is the most prominent at the earliest stage of their evolution (saturation regime). After this stage, the XUV luminosity decreases with time. For a 1 $M_\odot$ star, we estimate that the saturation regime lasts 30 Myr and emits 1.1×10^{31} erg s^{-1} of XUV (Sanz-Forcada et al. 2011), resulting in a mass loss rate of 6.9 $M_\oplus$ Gyr^{-1} for TOI-2196 b. While the XUV irradiation decreases with time after the saturation regime, it continues to contribute to atmospheric losses over ∼1 Gyr. To quantify this effect, we followed the approach of Aguichine et al. (2021) and integrated the average XUV radiation produced by a 1 $M_\odot$ star (Sanz-Forcada et al. 2011), assuming that the planet properties remained roughly constant during its evolution. With an efficiency of 5% (see Fig. 13 of Owen & Jackson 2012), we found that TOI-2196 b has lost ∼0.8 $M_\oplus$ of H/He. This implies that TOI-2196 b could have formed with a volatile mass fraction of 4–6%, and lost 50% to 90% of its atmosphere, a result that is consistent with the findings of Estrela et al. (2020).

Rapidly rotating stars can have longer saturation regimes, lasting up to 300 Myr (Tu et al. 2015; Poppenhaeger et al. 2021). When setting the duration of the saturation regime to 300 Myr, that is, ten times longer than in the computation above, the planet receives almost ten times more XUV energy, thus increasing the

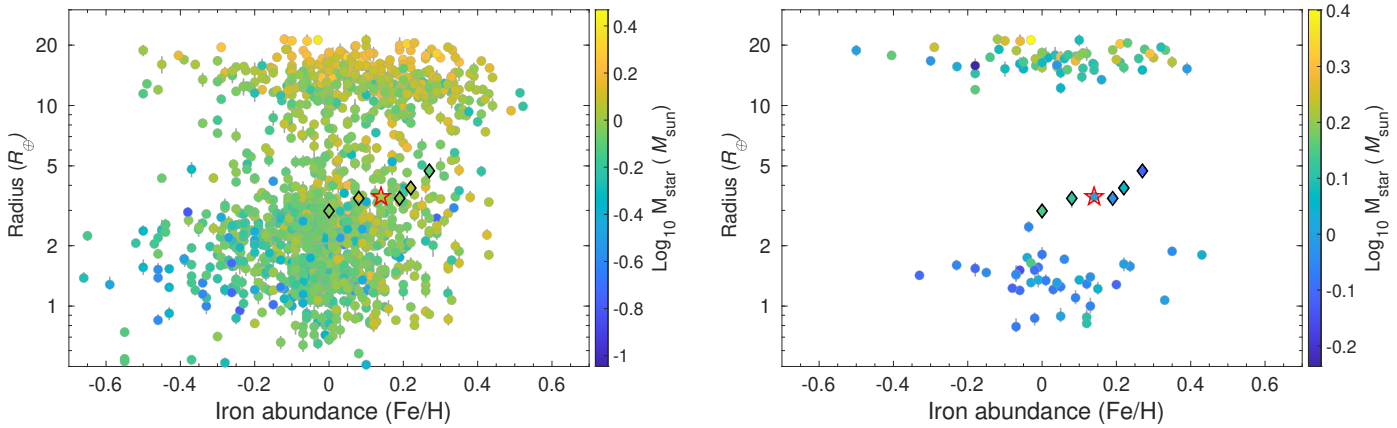

(a) (b)

Fig. 12. Planet radius vs. iron abundance diagram of the same planets as in Fig. 9: *a)* Colour-coded with stellar mass. *b)* Same but only plotting planets with $T_{eq} \geq 1800$ K, which corresponds to $P_{orb} \lesssim 1.3$ d for a sun-like star assuming zero Bond albedo and a heat redistribution factor of unity, or $P_{orb} \lesssim 0.43$ day for a K5 V star.

total lost mass by a factor of 10 (see Eq. (3)). In this extreme case, we estimate a mass loss corresponding to ~8 $M_\oplus$ of H/He envelope, placing the initial volatile mass fraction of TOI-2196 b at 35%. An envelope that massive contradicts the observed 1–10% range for sub-Neptunes, suggesting moderate or low activity levels for TOI-2196. However, these computations assume a constant planet mass and radius over time. The mass loss estimates should consider the coupling of the mass loss and interior structure. The apparent correlation between the planet age and the Jeans escape parameter Λ in Table 5 is supported by the study of Fossati et al. (2017). They found that planets with $\Lambda \geq 15$–35 experience important mass loss until their mass or radius (or both) adapts to increase Λ. We conclude that TOI-2196 b experienced atmospheric mass loss, which may still be taking place with a present-day mass loss rate of 0.01 $M_\oplus$ Gyr^{-1}. Its atmosphere has, however, not yet been removed entirely, placing it in the sub-Neptune category of exoplanets. The decrease in the mass-loss rate that prevented TOI-2196 b from losing its atmosphere could possibly be due to a change in the atmospheric composition. Atomic hydrogen, which can be produced by photo-dissociation of H_2 or H_2O, tends to escape at high rates mostly because of its low mass, but also because of its long radiative cooling time. A longer radiative cooling time implies that the gas will lose its heat through mechanical work, that is, through evaporative flow, rather than through radiation (Owen & Jackson 2012). A selective loss of H could result in atmospheres that are dominated by He, O_2, H_2O, or other heavy species with much lower escape rates (see Hu et al. 2015; Bolmont et al. 2017; Aguichine et al. 2021; Ito & Ikoma 2021, respectively). Since this planet inhabits a sparsely populated part of the radius versus equilibrium temperature diagram, it is a good candidate to study exceptions to the evaporation valley and evaporating planets in general.

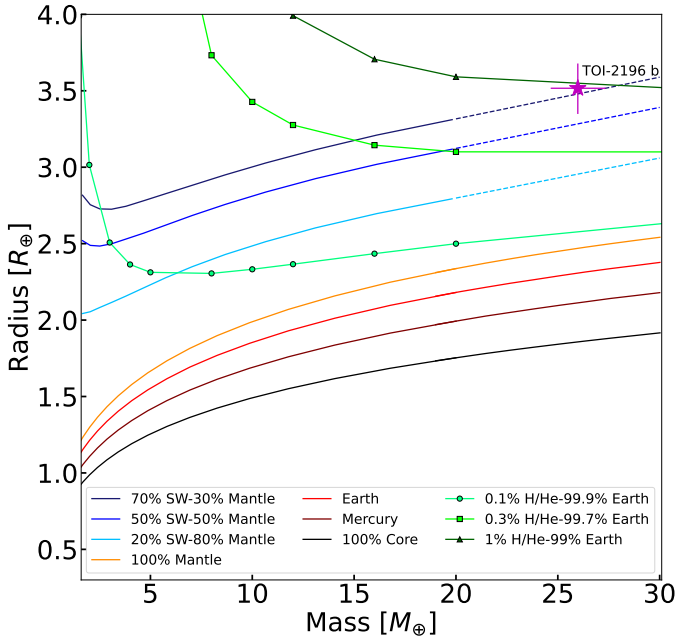

Fig. 13. Position of TOI-2196 b in the mass-radius diagram. We also show mass-radius relationships for dry planets with different core mass fractions (Brugger et al. 2016, 2017), water planets with varying supercritical water (SW) contents (Mousis et al. 2020; Acuña et al. 2021) and Earth-like cores with different H/He mass fractions (Zeng et al. 2019). We assume equilibrium temperatures of 1200 K and 2000 K for water planets and rocky planets with H/He atmospheres, respectively. Dashed lines indicate an extrapolation of the SW relations beyond their valid mass ranges. The lines for Earth, Mercury, and 100% core are lines of constant composition of respective type of planet.

4.3. Internal structure

If the composition of TOI-2196 b would partly include volatiles such as H/He or water, these elements would be in high-pressure and high-temperature phases due to the thickness of the volatile envelope. In Fig. 13, we compare TOI-2196 b with mass-radius relationships of planets with several different amounts of water in a supercritical state calculated with the model presented in Mousis et al. (2020) and Acuña et al. (2021), and with those of rocky planets with gaseous H/He atmospheres (Zeng et al. 2019). TOI-2196 b lies slightly above the 70% supercritical water (SW) composition under the assumption of a 100% mantle bulk. If we were to assume a core mass fraction (CMF) in agreement with its host stellar abundances (Table 6), the water content would increase since we would have to fit a similar total density with a more dense core. A water mass fraction (WMF) of ≃70% is

Table 6. MCMC parameters of the interior structure analysis and their 1 σ confidence intervals for scenario 1 (planet mass and radius as input) and scenario 2 (Fe/Si mole ratio in addition to mass and radius as input).

Parameter	Scenario 1	Scenario 2
CMF [(a)]	$\mathcal{U}(0,1)$	$0.244^{+0.057}_{-0.049}$
CRF [(b)]	$0.45^{+0.05}_{-0.14}$	$0.31^{+0.03}_{-0.02}$
$x_{\mathrm{H/He}}$ [(c)]	$0.0077^{+0.0094}_{-0.0032}$	$0.0066^{+0.0031}_{-0.0020}$
M ($M_\oplus$)	26.031±1.389	$25.998^{+1.410}_{-1.360}$
R ($R_\oplus$)	3.517±0.170	$3.470^{+0.202}_{-0.127}$
Fe/Si	$6.261^{+11.538}_{-6.261}$	0.747±0.175
z_{atm} [(d)] (km)	8143^{+1662}_{-1289}	7185^{+1298}_{-840}

Notes. [(a)]Core mass fraction. [(b)]Core radius fraction simultaneously computed with the CMF. [(c)]Hydrogen and helium mass fraction. [(d)]Planet atmosphere thickness.

similar to the maximum water content found in Solar System bodies (McKay et al. 2019). Thus, the atmosphere of TOI-2196 b is likely to be dominated by H/He which are less dense than water; otherwise, the water content of TOI-2196 b would be unrealistically high.

We therefore performed a MCMC Bayesian analysis (Acuña et al. 2021; Director et al. 2017) of the internal composition of TOI-2196 b assuming a H/He atmosphere. Following Brugger et al. (2016, 2017), we included two layers: an Fe-rich core and a silicate-rich mantle. To the calculated radius of the interior, we added the thickness of the H/He atmosphere, z_{atm}, to estimate the total planetary radius. We obtained the atmospheric thickness by subtracting the radius of a bare Earth-like core from the mass-radius relationships of an Earth-like core with a H/He atmosphere, presented by Zeng et al. (2019). The atmospheric thickness is then a function of the surface gravity, $g_0 = GM/R^2$, where G is the gravitational constant, and the H/He mass fraction, $z_{\mathrm{atm}} = z_{\mathrm{atm}}(g_0, x_{\mathrm{H/He}})$. We set the surface conditions for the interior model as 2000 K and 1 bar, since Zeng et al. (2019) considered an isothermal temperature profile for their atmosphere. Changing our surface pressure to other values would have a trivial effect on our interior bulk radius, since this parameter does not have an influence on the total radius of solid mantle–core planets (Otegi et al. 2020).

We considered two scenarios to obtain the interior structure of TOI-2196 b. Scenario 1 uses the planet mass and radius as input to the MCMC analysis, while scenario 2 also uses the stellar Fe/Si and Mg/Si mole ratios (Table 2) as input. To compute the Fe/Si and Mg/Si mole ratios with the stellar abundances, we follow the approach depicted in Brugger et al. (2017) and Sotin et al. (2007) and obtain Fe/Si = 0.775 ± 0.170 and Mg/Si = 1.192 ± 0.337. The MCMC analysis yields posterior distribution functions (PDF) of the core mass fraction and the H/He mass fraction.

The CMF and the H/He mass fraction, $x_{\mathrm{H/He}}$, represent our free parameters in the MCMC analysis. The CMF in scenario 1 is sampled as a uniform distribution between 0 and 1 which are the minimum and maximum values of the compositional parameters. In scenario 2, the CMF is constrained by the inclusion of the Fe/Si mole ratio as an input to the MCMC framework. This results in a mean value of the CMF of $0.244^{+0.057}_{-0.049}$ (Table 6) which is slightly lower than the CMF of Earth (0.32). The Earth value is, however, approximately at the limit of its 1 σ confidence interval as seen in Fig. 14. These results from scenario 2 are expected

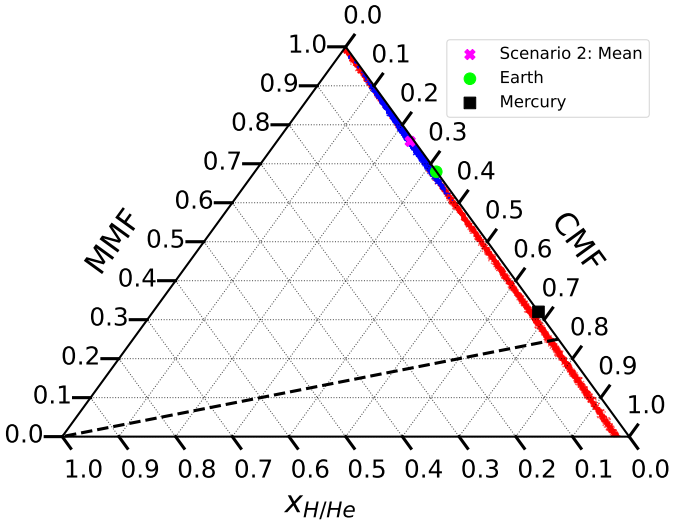

Fig. 14. Ternary diagram of the MCMC models for TOI-2196 b in scenario 1 (red), with the planet mass and the radius as input to the model, and in scenario 2 (blue), where also the stellar abundances are included. The mantle mass fraction (MMF) is defined as MMF = 1 − CMF − $x_{\mathrm{H/He}}$ where the latter parameter is the H/He mass fraction and CMF is the core mass fraction. The green circle and black square indicate the position of Earth and Mercury in the ternary diagram, respectively. The maximum CMF constrained by planet formation is limited by the black dashed line (see Sect. 4.3).

since the Fe/Si mole ratio of TOI-2196 b is lower than the solar value (0.96). The resulting mean value of the H/He mass fraction, $x_{\mathrm{H/He}}$, is approximately 0.7% in both scenarios. In the case of scenario 2, the uncertainties are lower than in scenario 1. This is due to the use of the Fe/Si mole ratio, which breaks the degeneracy between the CMF and the H/He mass fraction in scenario 2. Both scenarios agree that the minimum volatile mass fraction is ≃ 0.4%. In addition, we can consider scenario 1 as the most conservative one to derive the maximum volatile mass fraction for TOI-2196 b. The maximum CMF estimated from the protosolar nebula composition (Lodders et al. 2009) is 0.75. We mark this limit as a black dashed line in the ternary diagram in Fig. 14. We estimated the maximum volatile mass fraction as the $x_{\mathrm{H/He}}$ at which this line crosses the red points that correspond to the MCMC simulations in scenario 1, which is approximately 3%.

In Sect. 4.2, we show that the past volatile mass fraction of TOI-2196 b was approximately 4–6%, with an accompanying increase in mass of 0.8 $M_\oplus$. The radius for a planet of such mass and volatile mass fraction would be around 6 $R_\oplus$, according to the mass–radius relation of 5% H/He from Zeng et al. (2019), which changes the density from 3.3 g cm^{-3} to 0.7 g cm^{-3}. This shifts the position of TOI-2196 b in the density diagram in Fig. 11 downwards to the Saturn density with the difference of having a much lower mass than the gas giants in this parameter space. If we place the planet with the past radius and mass in the mass-radius diagram, it would be slightly above the small group of planets that includes LTT 9779 b, K2-100 b, and TOI-849 b, but still located in the hot Neptune desert and would still be classified as a planet in the Neptune regime, not a gaseous giant.

5. Conclusions

We present the detection and the analysis of the hot and volatile rich planet TOI-2196 b. It is smaller than Neptune but 50% more

massive resulting in a high bulk density for this type of planet. Another interesting result is the presence of a longer period body in this system detected in the radial velocity measurements as a linear trend with a minimum mass of ~0.65 M_J, assuming zero eccentricity. The outer body may be a warm or cold gas-giant planet, although a brown dwarf, or a very low-mass stellar companion, cannot be fully excluded at the present stage. A future long-term RV monitoring of the star is needed to determine the true nature of the signal. We estimate the mass loss of volatiles for planet b at a young age and find that while the mass loss could have been significant, the planet has not changed in terms of its character. It formed as a small volatile-rich planet and has remained one until today. The high equilibrium temperature of 1860 K, together with its radius and mass, places TOI-2196 b in the hot Neptune desert as a member of a very small population found so far. This small population suggests that the desert is divided in two parts: a hot sub-Neptune desert ($R_p \approx 1.8$–$3\ R_\oplus$) and a sub-Jovian desert ($R_p \approx 5$–$12\ R_\oplus$). However, more planets are needed for further studies for this special region.

Acknowledgements. This paper includes data collected by the TESS mission. Funding for the TESS mission is provided by the NASA Explorer Program. We acknowledge the use of public TESS data from pipelines at the TESS Science Office and at the TESS Science Processing Operations Center. Resources supporting this work were provided by the NASA High-End Computing (HEC) Program through the NASA Advanced Supercomputing (NAS) Division at Ames Research Center for the production of the SPOC data products. This work makes use of observations from the LCOGT network. Part of the LCOGT telescope time was granted by NOIRLab through the Mid-Scale Innovations Program (MSIP). This work uses observations made with ESO 3.6-m telescope at La Silla Observatory under programme ID 106.21TJ.001. We are grateful to the ESO staff members for their support during the observations, and to François Bouchy and Xavier Dumusque for coordinating the HARPS time sharing agreement. This work has made use of SME package, which benefits from the continuing development work by J. Valenti and N. Piskunov and we gratefully acknowledge their continued support. (Kupka et al. 2000; Ryabchikova et al. 2015). to page 5 C.M.P., M.F., I.G., and J.K. gratefully acknowledges the support of the Swedish National Space Agency (DNR 65/19, 174/18, 177/19, 2020-00104). L.M.S and D.G. gratefully acknowledge financial support from the CRT foundation under Grant No. 2018.2323 "Gaseous or rocky? Unveiling the nature of small worlds". P.K. acknowledges support from grant LTT-20015. E.G. acknowledges the support of the Thüringer Ministerium für Wirtschaft, Wissenschaft und Digitale Gesellschaft. J.S.J. greatfully acknowledges support by FONDECYT grant 1201371 and from the ANID BASAL projects ACE210002 and FB210003. H.J.D. acknowledges support from the Spanish Research Agency of the Ministry of Science and Innovation (AEI-MICINN) under grant PID2019-107061GB-C66, DOI: 10.13039/501100011033. D.D. acknowledges support from the TESS Guest Investigator Program grants 80NSSC21K0108 and 80NSSC22K0185. M.E. acknowledges the support of the DFG priority program SPP 1992 "Exploring the Diversity of Extrasolar Planets" (HA 3279/12-1). K.W.F.L. was supported by Deutsche Forschungsgemeinschaft grants RA714/14-1 within the DFG Schwerpunkt SPP 1992, Exploring the Diversity of Extrasolar Planets. N.N. acknowledges support from JSPS KAKENHI Grant Number JP18H05439, JST CREST Grant Number JPMJCR1761. M.S.I.P. is funded by NSF.

References

Acuña, L., Deleuil, Magali, Mousis, Olivier, et al. 2021, A&A, 647, A53
Adams, F. C., & Laughlin, G. 2006, ApJ, 649, 1004
Aguichine, A., Mousis, O., Deleuil, M., & Marcq, E. 2021, ApJ, 914, 84
Aguirre Børsen-Koch, V., Rørsted, J. L., Justesen, A. B., et al. 2022, MNRAS, 509, 4344
Allard, F., Homeier, D., & Freytag, B. 2012, Philos. Trans. Roy. Soc. Lond. A, 370, 2765
Anglada-Escudé, G., & Butler, R. P. 2012, ApJS, 200, 15
Armstrong, D. J., Lopez, T. A., Adibekyan, V., et al. 2020, Nature, 583, 39
Baranne, A., Queloz, D., Mayor, M., et al. 1996, A&AS, 119, 373
Barragán, O., Aigrain, S., Kubyshkina, D., et al. 2019a, MNRAS, 490, 698
Barragán, O., Gandolfi, D., & Antoniciello, G. 2019b, MNRAS, 482, 1017
Barragán, O., Aigrain, S., Rajpaul, V. M., & Zicher, N. 2022a, MNRAS, 509, 866
Barragán, O., Armstrong, D. J., Gandolfi, D., et al. 2022b, MNRAS, 514, 1606
Benítez-Llambay, P., Masset, F., & Beaugé, C. 2011, A&A, 528, A2
Berger, T. A., Huber, D., Gaidos, E., & van Saders, J. L. 2018, ApJ, 866, 99
Bolmont, E., Selsis, F., Owen, J. E., et al. 2017, MNRAS, 464, 3728
Borucki, W. J., Koch, D., Basri, G., et al. 2010, Science, 327, 977
Bowler, B. P. 2016, PASP, 128, 102001
Brown, T. M., Baliber, N., Bianco, F. B., et al. 2013, PASP, 125, 1031
Brugger, B., Mousis, O., Deleuil, M., & Lunine, J. I. 2016, ApJ, 831, L16
Brugger, B., Mousis, O., Deleuil, M., & Deschamps, F. 2017, ApJ, 850, 93
Bruntt, H., De Cat, P., & Aerts, C. 2008, A&A, 478, 487
Cabrera, J., Csizmadia, S., Erikson, A., Rauer, H., & Kirste, S. 2012, A&A, 548, A44
Castelli, F., & Kurucz, R. L. 2004, ArXiv e-prints [astro-ph/0405087]
Charbonneau, D., Allen, L. E., Megeath, S. T., et al. 2005, ApJ, 626, 523
Chen, H., & Rogers, L. A. 2016, ApJ, 831, 180
Choi, J., Dotter, A., Conroy, C., et al. 2016, ApJ, 823, 102
Claret, A. 2017, A&A, 600, A30
Claret, A., Hauschildt, P. H., & Witte, S. 2013, A&A, 552, A16
Collins, K. 2019, American Astronomical Society Meeting Abstracts, 233, 140.05
Collins, K. A., Kielkopf, J. F., Stassun, K. G., & Hessman, F. V. 2017, AJ, 153, 77
da Silva, L., Girardi, L., Pasquini, L., et al. 2006, A&A, 458, 609
Director, H. M., Gattiker, J., Lawrence, E., & Wiel, S. V. 2017, J. Stat. Comput. Simul., 87, 3521
Doyle, A. P., Davies, G. R., Smalley, B., Chaplin, W. J., & Elsworth, Y. 2014, MNRAS, 444, 3592
Erkaev, N. V., Kulikov, Y. N., Lammer, H., et al. 2007, A&A, 472, 329
Estrela, R., Swain, M. R., Gupta, A., Sotin, C., & Valio, A. 2020, ApJ, 898, 104
Findeisen, K., Hillenbrand, L., & Soderblom, D. 2011, AJ, 142, 23
Foreman-Mackey, D., Hoyer, S., Bernhard, J., & Angus, R. 2014, https://doi.org/10.5281/zenodo.11989
Fossati, L., Erkaev, N. V., Lammer, H., et al. 2017, A&A, 598, A90
Fridlund, M., Gaidos, E., Barragán, O., et al. 2017, A&A, 604, A16
Fulton, B. J., Petigura, E. A., Howard, A. W., et al. 2017, AJ, 154, 109
Georgieva, I. Y., Persson, C. M., Barragán, O., et al. 2021, MNRAS, 505, 4684
Ginzburg, S., Schlichting, H. E., & Sari, R. 2018, MNRAS, 476, 759
Gregory, P. C. 2005, ApJ, 631, 1198
Gupta, A., & Schlichting, H. E. 2019, MNRAS, 487, 24
Hidalgo, S. L., Pietrinferni, A., Cassisi, S., et al. 2018, ApJ, 856, 125
Hu, R., Seager, S., & Yung, Y. L. 2015, ApJ, 807, 8
Husser, T. O., Wende-von Berg, S., Dreizler, S., et al. 2013, A&A, 553, A6
Ito, Y., & Ikoma, M. 2021, MNRAS, 502, 750
Jenkins, J. M. 2002, ApJ, 575, 493
Jenkins, J. M., Chandrasekaran, H., McCauliff, S. D., et al. 2010, SPIE Conf. Ser., 7740, 77400D
Jenkins, J. M., Twicken, J. D., McCauliff, S., et al. 2016, SPIE Conf. Ser., 9913, 99133E
Jenkins, J. M., Tenenbaum, P., Seader, S., et al. 2020a, Kepler Data Processing Handbook: Transiting Planet Search, Kepler Science Document KSCI-19081-003
Jenkins, J. S., Díaz, M. R., Kurtovic, N. T., et al. 2020b, Nat. Astron., 4, 1148
Jin, S., Mordasini, C., Parmentier, V., et al. 2014, ApJ, 795, 65
Kempton, E. M. R., Bean, J. L., Louie, D. R., et al. 2018, PASP, 130, 114401
Kipping, D. M. 2013, MNRAS, 435, 2152
Kubyshkina, D., Lendl, M., Fossati, L., et al. 2018, A&A, 612, A25
Kuerster, M., Schmitt, J. H. M. M., Cutispoto, G., & Dennerl, K. 1997, A&A, 320, 831
Kupka, F. G., Ryabchikova, T. A., Piskunov, N. E., Stempels, H. C., & Weiss, W. W. 2000, Baltic Astron., 9, 590
Kurucz, R. L. 1993, VizieR Online Data Catalog: VI/39
Kurucz, R. L. 2013, ATLAS12: Opacity sampling model atmosphere program, Astrophysics Source Code Library [record ascl:1303.024]
Li, J., Tenenbaum, P., Twicken, J. D., et al. 2019, PASP, 131, 024506
Livingston, J. H., Crossfield, I. J. M., Petigura, E. A., et al. 2018, AJ, 156, 277
Lodders, K., Palme, H., & Gail, H. P. 2009, Landolt Börnstein, 4B, 712
Lopez, E. D., & Fortney, J. J. 2013, ApJ, 776, 2
Lopez, E. D., & Fortney, J. J. 2014, ApJ, 792, 1
Lovis, C., & Pepe, F. 2007, A&A, 468, 1115
Lundkvist, M. S., Kjeldsen, H., Albrecht, S., et al. 2016, Nat. Commun., 7, 11201
Mamajek, E. E., & Hillenbrand, L. A. 2008, ApJ, 687, 1264
Mandel, K., & Agol, E. 2002, ApJ, 580, L171
Mayor, M., Pepe, F., Queloz, D., et al. 2003, The Messenger, 114, 20
Mazeh, T., Nachmani, G., Holczer, T., et al. 2013, ApJS, 208, 16
Mazeh, T., Holczer, T., & Faigler, S. 2016, A&A, 589, A75

McCully, C., Volgenau, N. H., Harbeck, D.-R., et al. 2018, SPIE Conf. Ser., 10707, 107070K
McKay, A. J., DiSanti, M. A., Kelley, M. S. P., et al. 2019, AJ, 158, 128
Mousis, O., Deleuil, M., Aguichine, A., et al. 2020, ApJ, 896, L22
Otegi, J. F., Dorn, C., Helled, R., et al. 2020, A&A, 640, A135
Owen, J. E., & Jackson, A. P. 2012, MNRAS, 425, 2931
Owen, J. E., & Lai, D. 2018, MNRAS, 479, 5012
Owen, J. E., & Wu, Y. 2013, ApJ, 775, 105
Parviainen, H. 2015, MNRAS, 450, 3233
Pepe, F., Mayor, M., Galland, F., et al. 2002, A&A, 388, 632
Persson, C. M., Fridlund, M., Barragán, O., et al. 2018, A&A, 618, A33
Petigura, E. A., Rogers, J. G., Isaacson, H., et al. 2022, AJ, 163, 179
Piskunov, N., & Valenti, J. A. 2017, A&A, 597, A16
Poppenhaeger, K., Ketzer, L., & Mallonn, M. 2021, MNRAS, 500, 4560
Ricker, G. R., Winn, J. N., Vanderspek, R., et al. 2015, J. Astron. Telescopes Instrum. Syst., 1, 014003
Ryabchikova, T., Piskunov, N., Kurucz, R. L., et al. 2015, Phys. Scr, 90, 054005
Sanchis-Ojeda, R., Rappaport, S., Winn, J. N., et al. 2014, ApJ, 787, 47
Sanz-Forcada, J., Micela, G., Ribas, I., et al. 2011, A&A, 532, A6
Schlegel, D. J., Finkbeiner, D. P., & Davis, M. 1998, ApJ, 500, 525
Smith, A. M. S., Gandolfi, D., Barragán, O., et al. 2017, MNRAS, 464, 2708
Sotin, C., Grasset, O., & Mocquet, A. 2007, Icarus, 191, 337
Stumpe, M. C., Smith, J. C., Catanzarite, J. H., et al. 2014, PASP, 126, 100
Szabó, G. M., & Kiss, L. L. 2011, ApJ, 727, L44
Tokovinin, A. 2018, PASP, 130, 035002
Tu, L., Johnstone, C. P., Güdel, M., & Lammer, H. 2015, A&A, 577, A3
Twicken, J. D., Catanzarite, J. H., Clarke, B. D., et al. 2018, PASP, 130, 064502
Valenti, J. A., & Piskunov, N. 1996, A&AS, 118, 595
Van Eylen, V., Agentoft, C., Lundkvist, M. S., et al. 2018, MNRAS, 479, 4786
Van Eylen, V., Astudillo-Defru, N., Bonfils, X., et al. 2021, MNRAS, 507, 2154
Vines, J. I., & Jenkins, J. S. 2022, MNRAS, 513, 2719
Yee, S. W., Petigura, E. A., & von Braun, K. 2017, ApJ, 836, 77
Zechmeister, M., & Kürster, M. 2009, A&A, 496, 577
Zechmeister, M., Reiners, A., Amado, P. J., et al. 2018, A&A, 609, A12
Zeng, L., Jacobsen, S. B., Sasselov, D. D., et al. 2019, Proc. Natl. Acad. Sci., 116, 9723
Ziegler, C., Tokovinin, A., Briceño, C., et al. 2020, AJ, 159, 19

[1] Department of Space, Earth and Environment, Chalmers University of Technology, Onsala Space Observatory, 439 92 Onsala, Sweden
e-mail: carina.persson@chalmers.se
[2] Dipartimento di Fisica, Universita degli Studi di Torino, via Pietro Giuria 1, 10125 Torino, Italy
[3] Aix Marseille Université, Institut Origines, CNRS, CNES, LAM, Marseille, France
[4] Department of Space, Earth and Environment, Chalmers University of Technology, Chalmersplatsen 4, 412 96 Gothenburg, Sweden
[5] Thüringer Landessternwarte Tautenburg, Sternwarte 5, 07778 Tautenburg, Germany
[6] Astrobiology Center, 2-21-1 Osawa, Mitaka, Tokyo 181-8588, Japan
[7] National Astronomical Observatory of Japan, 2-21-1 Osawa, Mitaka, Tokyo 181-8588, Japan
[8] Department of Astronomy, The Graduate University for Advanced Studies (SOKENDAI), 2-21-1 Osawa, Mitaka, Tokyo, Japan
[9] Center for Astrophysics, Harvard & Smithsonian, 60 Garden Street, Cambridge, MA 02138, USA
[10] Division of Geological and Planetary Sciences, 1200 E California Blvd, Pasadena, CA 91125, USA
[11] Leiden Observatory, University of Leiden, PO Box 9513, 2300 RA Leiden, The Netherlands
[12] Núcleo de Astronomía, Facultad de Ingeniería y Ciencias, Universidad Diego Portales, Av. Ejército 441, Santiago, Chile
[13] Centro de Astrofísica y Tecnologías Afines (CATA), Casilla 36-D, Santiago, Chile
[14] Astronomical Institute of the Czech Academy of Sciences, Fričova 298, 25165 Ondřejov, Czech Republic
[15] Department of Physics and Kavli Institute for Astrophysics and Space Research, Massachusetts Institute of Technology, Cambridge, MA 02139, USA
[16] Sub-department of Astrophysics, Department of Physics, University of Oxford, Oxford OX1 3RH, UK
[17] Instituto de Astrofísica de Canarias, C. Via Lactea S/N, E-38205 La Laguna, Tenerife, Spain
[18] NASA Goddard Space Flight Center, Exoplanets and Stellar Astrophysics Laboratory (Code 667), Greenbelt, MD 20771, USA
[19] McDonald Observatory and Center for Planetary Systems Habitability, The University of Texas, Austin, TX USA
[20] Caltech/IPAC-NASA Exoplanet Science Institute, 770 S. Wilson Avenue, Pasadena, CA 91106, USA
[21] Universidad de La Laguna, Dept. de Astrofísica, 38206 La Laguna, Tenerife, Spain
[22] Department of Physics and Astronomy, University of New Mexico, 210 Yale Blvd NE, Albuquerque, NM 87106, USA
[23] Department of Astronomy and Tsinghua Centre for Astrophysics, Tsinghua University, Beijing 100084, PR China
[24] Rheinisches Institut für Umweltforschung an der Universität zu Köln, Aachener Strasse 209, 50931 Köln, Germany
[25] SUPA Physics and Astronomy, University of St. Andrews, Fife KY16 9SS Scotland, UK
[26] NASA Ames Research Center, Moffett Field, CA 94035, USA
[27] Department of Physics and Astronomy, University of Louisville, Louisville, KY 40292, USA
[28] Freie Universität Berlin, Institute of Geological Sciences, Malteserstr. 74-100, 12249 Berlin, Germany
[29] Institute of Planetary Research, German Aerospace Center (DLR), Rutherfordstrasse 2, 12489 Berlin, Germany
[30] Department of Astronomy & Astrophysics, University of Chicago, Chicago, IL 60637, USA
[31] Astrophysics Group, Cavendish Laboratory, University of Cambridge, J.J. Thomson Avenue, Cambridge CB3 0HE, UK
[32] Kavli Institute for Cosmology, University of Cambridge, Madingley Road, Cambridge CB3 0HA, UK
[33] Komaba Institute for Science, The University of Tokyo, 3-8-1 Komaba, Meguro, Tokyo 153-8902, Japan
[34] Mullard Space Science Laboratory, University College London, Holmbury St Mary, Dorking, Surrey RH5 6NT, UK
[35] Wild Boar Remote Observatory, San Casciano in val di Pesa, Firenze, 50026, Italy
[36] Department of Earth, Atmospheric, and Planetary Sciences, Massachusetts Institute of Technology, Cambridge, MA 02139, USA
[37] Department of Aeronautics and Astronautics, Massachusetts Institute of Technology, Cambridge, MA 02139, USA
[38] Department of Physics & Astronomy, Vanderbilt University, Nashville, TN 37235, USA
[39] Tsinghua International School, Beijing 100084, PR China
[40] Department of Astrophysical Sciences, Princeton University, Princeton, NJ 08544, USA
[41] SETI Institute, Mountain View, CA 94043, USA
[42] Societá Astronomica Lunae, Castelnuovo Magra, Italy
[43] Department of Physics, Engineering and Astronomy, Stephen F. Austin State University, 1936 North St, Nacogdoches, TX 75962, USA

Appendix A: HARPS data

Table A.1: Radial velocities and spectral activity indicators extracted from HARPS spectra.

BJD_{TBD} (days) -2457000	RV ($m\,s^{-1}$)	σ_{RV} ($m\,s^{-1}$)	BIS[a] ($m\,s^{-1}$)	FHWM ($km\,s^{-1}$)	σ_{FWHM} ($km\,s^{-1}$)	dlW ($km\,s^{-1}$)	σ_{dlW} ($km\,s^{-1}$)	S-index —	$\sigma_{S-index}$ —	H_α [a] —	T_{exp} (s)	SNR @550 nm
2419.661798	0.016377394	0.002998808	-0.029284737	7.140376417	0.357018821	11.22278765	1.846614321	0.172559779	0.003497890	0.998197146	2100	28.4
2419.812144	0.020510551	0.002956139	-0.014619464	7.138481028	0.356924051	11.05843113	2.062412649	0.181116594	0.003877305	0.999901855	2100	29.1
2424.705788	0.018156264	0.002574676	-0.006295520	7.137545136	0.356877257	-1.018335758	1.512092568	0.160211164	0.002998846	0.995506908	2400	33.5
2427.626567	-0.000481393	0.001746737	-0.014103206	7.137688356	0.356884418	-8.910686514	1.508117865	0.162656713	0.002592005	1.005319679	2400	38.5
2427.810834	0.014869853	0.002302020	-0.014228541	7.151375312	0.357568766	-7.928578176	1.652097812	0.172320637	0.003198341	1.003490323	2400	37.9
2428.639266	-0.009267622	0.002545470	-0.011727208	7.143755477	0.357187774	2.109340183	1.791528912	0.161061807	0.003508646	0.989901071	2400	28.1
2428.720190	-0.009409333	0.002468478	-0.014294956	7.143700306	0.357185015	-5.089153308	1.945891805	0.164078903	0.003161212	0.985814569	2100	25.7
2428.793337	-0.005702919	0.003047684	-0.017037973	7.147611628	0.357380581	-0.909110563	1.543522493	0.171465389	0.004068059	0.988770164	2100	28.1
2429.600426	0.005566032	0.002201269	-0.022909545	7.142051926	0.357102596	-3.451494525	1.456484985	0.177564159	0.003168727	0.990316656	2400	32.4
2429.701720	-0.005281992	0.002460195	-0.018750634	7.154825057	0.357741253	-2.086622561	1.290738998	0.172611870	0.003022147	0.986268731	2400	31.1
2429.779264	-0.003881037	0.002363704	-0.003667828	7.149787004	0.357489350	-2.847121560	1.483978769	0.182034670	0.003499536	0.999352266	2400	31.7
2430.605449	0.020690196	0.002615154	-0.026428800	7.140959158	0.357047958	-0.876773808	1.898119925	0.170006651	0.003561435	0.988708161	2400	28.5
2430.675216	0.009714846	0.003448313	-0.029337161	7.142366435	0.357118322	3.997268509	2.841797354	0.156868483	0.004172708	1.009883115	2400	22.7
2430.793963	0	0.004101949	-0.014566066	7.154824695	0.357741235	17.76124298	2.793467679	0.152186686	0.005026666	0.990507323	2400	19.5
2432.708547	0.010934787	0.002813860	-0.017938111	7.142515648	0.357125782	3.522072813	2.007823948	0.173702481	0.004060536	0.996595505	2100	26.7
2432.771624	0.020807163	0.003165590	0.005396245	7.146888465	0.357344423	1.482052001	2.180986562	0.197696011	0.004567345	1.000737242	2400	25.7
2433.589404	-0.005759122	0.004543362	-0.012638667	7.141966902	0.357098345	13.73210968	3.238231507	0.156301540	0.004919294	1.005853124	2400	18.4
2460.511224	0.005895298	0.002957171	-0.023272945	7.138558338	0.356927917	0.173120003	2.294055305	0.160858365	0.003977862	0.990624216	2400	24.2
2460.703136	-0.006202675	0.002962588	-0.018801690	7.132139304	0.356606965	1.994551964	2.507608654	0.167471110	0.004007204	0.996410287	2400	26.6
2461.528107	0.015996184	0.002325161	-0.025352893	7.120917671	0.356045884	-4.356761078	1.674535666	0.167688344	0.003392494	0.993608739	2400	29.1
2461.603775	0.019667017	0.003719634	-0.019049084	7.139453642	0.356972682	6.047329254	2.393000701	0.234380548	0.005077442	0.985384534	2700	23.5
2462.548288	0.004650384	0.002753746	-0.013112217	7.148418697	0.357420935	-2.298627181	1.835342272	0.163604136	0.003269482	1.003634973	2400	28.8
2462.697690	0.019120366	0.002733685	-0.023693674	7.140938077	0.357046904	1.663468315	2.176539325	0.163773867	0.003736499	1.005965119	2400	28.4
2463.523956	-0.007480005	0.004354283	0.003485374	7.122732003	0.356136600	12.53839580	2.886964792	0.246356354	0.005634937	0.984976420	2400	21.3
2463.686332	0.004361950	0.002607838	-0.022706813	7.151924899	0.357596245	4.120020246	2.327407159	0.186998648	0.004292668	0.996282723	2400	25.9
2467.619853	0.012521115	0.002237602	-0.018435484	7.134447548	0.356722377	-4.351583321	1.134570545	0.170492054	0.003035039	0.998282998	2100	36.2
2470.576694	-0.014622498	0.003224917	-0.006783539	7.135561560	0.356778078	0.830073320	2.446677634	0.222651785	0.004940337	0.994695320	2400	24.7
2471.526954	-0.009509969	0.001711479	-0.016340895	7.135242022	0.356762101	-9.899564167	1.551739631	0.169208331	0.002841745	0.994933456	2400	38.4
2472.542615	-0.000106014	0.002917387	-0.016347214	7.121805322	0.356090266	5.079370467	2.249824118	0.170382224	0.003877015	0.994651399	2400	26.9
2473.515372	0.011278635	0.001998208	-0.014749743	7.145702914	0.357285146	-4.351123275	1.618986012	0.162113008	0.002889922	0.991353982	2400	35.4
2473.636500	0.008755525	0.002003567	-0.021534768	7.138369046	0.356918452	-9.531662223	1.359621503	0.187348591	0.003337473	0.994049878	2400	37.2
2474.557662	0.009871217	0.002272828	-0.020330444	7.141533353	0.357076668	-0.237590000	1.540770964	0.171545292	0.003304167	1.000336629	2400	32.2
2475.556563	-0.003711372	0.002152913	-0.015830215	7.147198245	0.357359912	0.211648000	1.715704638	0.174905076	0.003290315	1.011519561	2400	32.1
2475.670168	0.002865511	0.002723374	-0.010147531	7.136697027	0.356834851	8.052287871	2.305851198	0.175846935	0.004053048	0.992356017	2400	27.7
2476.559248	-0.020460820	0.003324717	-0.008768004	7.143915814	0.357195791	8.236826883	2.036921846	0.160440241	0.003685363	0.998942580	2400	26.4
2476.661638	-0.013027107	0.004830712	-0.014629884	7.111509280	0.355575464	45.07848938	3.356598711	0.183341839	0.005507660	0.999140509	2400	19.6
2477.552408	-0.014509429	0.005655293	-0.023830532	7.148861028	0.357443051	31.61015391	3.608882476	0.211182628	0.006363658	1.000245782	2400	16.9
2477.656210	-0.020161994	0.003897063	-0.038365216	7.144018458	0.357200923	16.59729732	2.786390384	0.201276239	0.005205999	0.988922086	2400	22.3
2478.601501	-0.007845141	0.002402883	-0.017684734	7.153895769	0.357694788	5.732488697	2.000829919	0.173492875	0.003579341	0.993562249	2400	30
2502.537972	-0.021841648	0.002927285	-0.014627725	7.121132243	0.356056612	1.435156202	1.865134741	0.194001634	0.004109944	0.998458563	2400	28.6
2530.516620	-0.020554079	0.002689375	-0.015004302	7.132953081	0.356647654	-2.396505538	1.873603833	0.183751932	0.003612815	0.993572861	2400	31.3

Notes. [a] We used 5% of the activity indicator as uncertainties.